Journal of Neuroinflammation

RESEARCH

Open Access

iPSC-derived PSEN2 (N141I) astrocytes and microglia exhibit a primed inflammatory phenotype

Michael A. Sullivan[1], Samuel D. Lane[1], André D. J. McKenzie[1], Sarah R. Ball[1], Margaret Sunde[1], G. Gregory Neely[2], Cesar L. Moreno[2], Alexandra Maximova[1], Eryn L. Werry[1,3,4*] and Michael Kassiou[3*]

Abstract

Background Widescale evidence points to the involvement of glia and immune pathways in the progression of Alzheimer's disease (AD). AD-associated iPSC-derived glial cells show a diverse range of AD-related phenotypic states encompassing cytokine/chemokine release, phagocytosis and morphological profiles, but to date studies are limited to cells derived from PSEN1, APOE and APP mutations or sporadic patients. The aim of the current study was to successfully differentiate iPSC-derived microglia and astrocytes from patients harbouring an AD-causative PSEN2 (N141I) mutation and characterise the inflammatory and morphological profile of these cells.

Methods iPSCs from three healthy control individuals and three familial AD patients harbouring a heterozygous PSEN2 (N141I) mutation were used to derive astrocytes and microglia-like cells and cell identity and morphology were characterised through immunofluorescent microscopy. Cellular characterisation involved the stimulation of these cells by LPS and $A\beta_{42}$ and analysis of cytokine/chemokine release was conducted through ELISAs and multi-cytokine arrays. The phagocytic capacity of these cells was then indexed by the uptake of fluorescently-labelled fibrillar $A\beta_{42}$.

Results AD-derived astrocytes and microglia-like cells exhibited an atrophied and less complex morphological appearance than healthy controls. AD-derived astrocytes showed increased basal expression of GFAP, S100β and increased secretion and phagocytosis of $A\beta_{42}$ while AD-derived microglia-like cells showed decreased IL-8 secretion compared to healthy controls. Upon immunological challenge AD-derived astrocytes and microglia-like cells showed exaggerated secretion of the pro-inflammatory IL-6, CXCL1, ICAM-1 and IL-8 from astrocytes and IL-18 and MIF from microglia.

Conclusion Our study showed, for the first time, the differentiation and characterisation of iPSC-derived astrocytes and microglia-like cells harbouring a PSEN2 (N141I) mutation. PSEN2 (N141I)-mutant astrocytes and microglia-like cells presented with a 'primed' phenotype characterised by reduced morphological complexity, exaggerated pro-inflammatory cytokine secretion and altered $A\beta_{42}$ production and phagocytosis.

Keywords Microglia, Astrocytes, Glia, Alzheimer's disease, Pro-inflammatory, iPSC, PSEN2, Amyloid-beta, Morphology

*Correspondence:
Eryn L. Werry
eryn.werry@sydney.edu.au
Michael Kassiou
michael.kassiou@sydney.edu.au
Full list of author information is available at the end of the article

Introduction

Alzheimer's disease (AD) is currently a largely unmet worldwide clinical burden, despite being the subject of many clinical trials over the last decade. AD occurs either as early onset familial AD (fAD) around the fourth decade of life or late-stage sporadic AD (sAD) which usually develops past 65 years old. sAD is the more common form of the disease (>95% frequency) with the biggest genetic risk factors for developing sAD including triggering receptor expressed on myeloid cells 2 (TREM2) and the ε4 allele of the Apolipoprotein E (APOE) gene [1]. fAD accounts for less than 5% of total AD cases and the causative mutations are inherited in an autosomal dominant fashion, with over 200 different mutations occurring in the amyloid precursor protein (APP), presenilin-1 (PSEN1) and presenilin-2 (PSEN2) genes [1, 2]. PSEN1/2 subunits are at the catalytic core of the γ-secretase complex and as such, mutations in these subunits are central to the amyloidogenic processing of APP within fAD [3, 4]. Currently, up to 18 pathogenic mutations have been identified in the *PSEN2* gene, with the N141I missense mutation being the most prevalent AD-causing PSEN2 mutation (comprising 70% of PSEN2-mutant AD patients) and presents with a high clinical penetrance (>95%) [5]. It is a mutation which impacts neuronal action potential properties [6]. The aetiology of AD is not well understood but both the sporadic and familial forms of the disease have common neuropathological features which most noticeably include gross brain atrophy, neuroinflammation, insoluble parenchymal amyloid-β (Aβ) deposits and intracellular neurofibrillary tangles containing hyperphosphorylated tau [7].

Increasing evidence suggests glial cells are central to disease-modifying dysfunctions in AD pathogenesis. Genome-wide association studies have identified several genetic risk loci that implicate the innate immune system in the development of AD [8]. Within the brain of AD patients, increased microglial activation is observed during the prodromal and potentially preclinical stages of AD and is present in both mildly and severely cognitively impaired individuals [9, 10]. Additionally, astrocytes in the post-mortem brain of AD patients exhibit significant cellular atrophy, upregulate the cytoskeletal protein glial fibrillary acidic protein (GFAP) and internalise Aβ [11–14]. While post-mortem studies find microglia and astrocytes surrounding Aβ aggregates in high numbers, this research fails to answer when and how microglia and astrocytes specifically respond to Aβ, and whether this is beneficial or detrimental for AD progression [15–17]. Furthermore, preclinical transgenic mouse models of AD are limited in their ability to imitate the early stages of the pathological cascade, show significant species differences to humans and show poor clinical translation of therapeutics [18]. As such, there remains a clear need to investigate cell-specific and cell-autonomous changes occurring early in disease progression, by examining human glial cells in vitro.

Induced pluripotent stem cell (iPSC)-derived CNS cells closely mimic their in vivo counterparts and provide a new opportunity to characterise AD-associated functions within these cells in vitro [19, 20]. Previous publications have reported the successful in vitro differentiation of iPSCs to microglia-like cells and astrocytes with high yield and purity [21–23]. iPSC-derived astrocytes and microglia-like cells from both sAD and fAD origin have been utilised to investigate a variety of AD-associated changes in morphology, cytokine/chemokine release and phagocytosis. Similarities between fAD-derived (*APP*- and *PSEN1*-mutant) and sAD-derived astrocytes and microglia include increased secretion of pro-inflammatory cytokines IL-6 and IL-8 in response to inflammatory stimuli. Common morphological changes including shorter and fewer cellular processes were observed between multiple AD-derived models of astrocytes and microglia. Despite these similarities, there is variability in chemoattractant secretion such as CCL2 and a number of other pro-inflammatory cytokines including tumour necrosis factor-α (TNF-α) across different AD patient origins [24–30]. Further variability between disease origin was observed when measuring the ability of microglia to phagocytose $A\beta_{42}$ or yeast bioparticles, finding fAD-derived microglia to increase uptake while sAD-associated microglia showed the opposite [25, 31]. The existing body of research suggests that iPSC-derived glial cells show complex behaviours, likely indicative of a diverse range of AD-related phenotypic states encompassing cytokine/chemokine release, phagocytosis and morphological profiles.

The existing body of research examining the molecular and cellular behaviour of iPSC-derived glia has focused on iPSCs established from APP, PSEN1 or sAD donors, with no studies having directly examined astrocytes/microglia derived from patients carrying PSEN2 mutations. Given the lack of research on iPSC-derived PSEN2 mutant glial cells, it is important to establish the AD-associated cellular characteristics of PSEN2-mutant astrocytes and microglia. This will provide further understanding of common inflammatory or other glial-specific mechanisms which may help guide drug discovery towards a pan-AD treatment. The aim of the current study was to successfully differentiate iPSC-derived microglia and astrocytes from patients harbouring a PSEN2 (N141I) mutation and investigate

the morphological, inflammatory and phagocytic phenotype presented.

Materials and methods

iPSC lines

Human control iPSCs were obtained from the Cedars-Sinai iPSC Core cell repository (Los Angeles, USA). Heterozygous fAD PSEN2 (N141I) iPSCs were obtained from both the Cedars-Sinai (Los Angeles, USA) and New York Stem-Cell Foundation cell repositories (New York, USA). All lines were generated from dermal fibroblasts obtained from skin punch biopsies, reprogrammed using either a non-integrating episomal plasmid or mRNA transfection and showed normal karyotyping. A summary of the iPSC line characteristics is shown in Table 1.

iPSC culture

iPSCs were cultured in feeder-free conditions on Matrigel-coated (0.08 mg/well) 6-well tissue culture plates in mTesR1 media (StemCell Technologies) at 37 ˚C and 5% CO_2. Cultures were fed daily. For passaging of iPSC cultures, differentiated colonies were manually scratched off the bottom of the well and media was aspirated. Fresh media was added and passaged 1:6 using the StemPro EZpassage tool (Life Technologies) as per the manufacturer's instructions.

NPC derivation

Derivation of neural progenitor cells (NPCs) from iPSCs closely followed a previously published protocol [23]. iPSCs were cultured with the addition of 10 ng/mL StemBeads fibroblast growth factor 2 (FGF-2) (StemCultures). Upon reaching 80% confluency, the media was changed to TeSR-E8 supplemented with 10 ng/mL StemBeads FGF-2 and 10 µM Y-27632 (Sigma-Aldrich). After 24 h, cells were washed with phosphate buffered saline (PBS), dissociated with gentle cell dissociation reagent (StemCell Technologies) and incubated for 10 min (37 °C, 5% CO_2). Cells were gently pipetted up and down to ensure all cells had dislodged and formed a single cell suspension. Cells were then centrifuged (300 g, 5 min) and plated at a density of 90,000 cells/mL in STEMdiff Neural Induction Medium (StemCell Technologies) with SMADi supplement (StemCell Technologies) (NIM) and 10 µM Y-27632 on an ultra-low attachment U-bottom 96-well plate (100 µL/well) (Costar) and incubated at 37 ˚C, 5% CO_2. Three-quarters of the media was changed daily for 4 days, ensuring the embryoid bodies were not removed. Embryoid bodies were aspirated using a 200 µL wide-bore pipette tip and plated onto Matrigel-coated (0.08 mg/well) 6-well plates (10–13 embryoid bodies/well) in NIM. Media was fully replaced daily for 7 days. Cells were washed with Dulbecco's Modified Eagle Medium (DMEM/F12) and incubated for 70 min (37 ˚C, 5% CO_2) in STEMdiff Neural Rosette Selection Reagent (StemCell Technologies). Rosettes were lifted by gently dispensing DMEM/F12 onto the colonies, centrifuged (350 g, 5 min), plated onto a Matrigel-coated (0.08 mg/well) 6-well plate in NIM and incubated for 24 h (37 ˚C, 5% CO_2). Media was switched to neural progenitor cell media containing DMEM/F12, 1×N2 (Invitrogen), 1×B27-RA (Invitrogen) and 20 ng/ml FGF_2 (Abcam) and changed daily. NPCs were passaged after 4 days using Accutase (Sigma-Aldrich) (5 min, 37 °C, 5% CO_2) and maintained on Matrigel-coated (0.08 mg/well) 6-well plates. Further passaging was done approximately 1:3 every week.

Astrocyte derivation

Differentiation of NPCs into astrocytes followed a previously published protocol [23]. NPCs were dissociated using accutase (5 min, 37 °C, 5% CO_2), centrifuged (300 g, 5 min), plated at 15,000 cells/cm^2 on Matrigel-coated (0.08 mg/well) 6-well plates in NPC medium and incubated for 24 h (37 °C, 5% CO_2). Media was switched to astrocyte medium (astrocyte basal medium

Table 1 Summary of iPSC line characteristics

iPSC line	Sex	Age at collection (years)	Disease status	APOE genotype[1]	Origin tissue	Reprogramming method
Ctrl-06	F	82	Healthy control	ε3/ε3	Fibroblast	Episomal plasmid
Ctrl-71	F	61	Healthy control	ε3/ε3	Fibroblast	Episomal plasmid
Ctrl-88	M	57	Healthy control	ε3/ε4	Fibroblast	Episomal plasmid
fAD-08	F	81	Alzheimer's(PSEN2 N141I)	ε3/ε3	Fibroblast	Episomal plasmid
fAD-948	F	40	Alzheimer's (PSEN2 N141I)	ε3/ε4	Fibroblast	mRNA
fAD-950	F	37	Alzheimer's (PSEN2 N141I)	ε3/ε4	Fibroblast	mRNA

iPSC induced pluripotent stem cell, *APOE* apolipoprotein, *PSEN2* presenilin 2 [1]APOE genotype determined by Sanger sequencing on genomic iPSC DNA (Additional file 1: Fig. S1)

(ScienCell), 2% fetal bovine serum, astrocyte growth supplement and 10 U/mL penicillin/streptomycin solution) and were fed every other day. Cells were passaged with accutase (5 min, 37 °C, 5% CO2) when reaching 90% confluency, centrifuged (300 g, 5 min) and plated at the original plating density. After 30 days in astrocyte medium, astrocyte identity was then validated using immunofluorescence and used for experiments.

Microglia derivation

Differentiation of iPSCs to hematopoietic progenitor cells (HPCs) was done using Stem Cell Technologies STEMdiff Hematopoietic Kit (StemCell Technologies). Upon reaching 80% confluency, iPSCs were detached using gentle cell dissociation reagent (StemCell Technologies) (10 min, 37 °C, 5% CO_2) and plated at 40 colonies/well on Matrigel-coated (0.08 mg/well) 12-well plates in mTeSR1 media (StemCell Technologies) supplemented with mTeSR1 5×Supplement (StemCell Technologies), ensuring the colony sizes were around 50–100 µm in diameter. The following day mTeSR1 medium was replaced with media A (Hematopoietic basal medium with supplement A at 1:200). After 48 h, a half media change was conducted with media A. Twenty-four hours later, media was switched to media B (Hematopoietic Basal Medium with supplement B at 1:200). A half media change was conducted 2, 4 and 7 days later, ensuring not to disturb the floating cell population. After 9 days in media B, media was completely removed and washed once with DMEM/F12 to ensure all non-adherent cells were collected. These cells were hematopoietic progenitor cells. The cell-containing supernatant was centrifuged (300 g, 5 min) and plated at 200,000 cells/well on Matrigel-coated (0.08 mg/well) 6-well plates containing 2 mL STEMdiff Microglia Differentiation Media (Microglia Basal Medium with supplement 1 at 1:10 and supplement 2 at 1:250). STEMdiff Microglia Differentiation Media (1 mL) was added every other day. After 12 days both the semi-adherent and non-adherent cells were collected, centrifuged (300 g, 5 min), resuspended in a 1:1 mixture of cell supernatant and fresh STEMdiff Microglia Differentiation Media and plated on a Matrigel-coated (0.08 mg/well) 6-well plate. STEMdiff Microglia Differentiation Media (1 mL) was added every other day for a further 12 days. Non-adherent cells were collected and adherent cells were detached using accutase (5 min, 37 °C, 5% CO_2), centrifuged (300 g, 5 min) and plated on Matrigel-coated surfaces (depending on application) at 100,000 cells/cm^2 in STEMdiff Microglia Maturation Media (STEMdiff Microglia Differentiation Media with supplement 3 at 1:250). Half of the initial plating media volume of STEMdiff Microglia Maturation Media was added every other day for 8 days, at which point the microglia-like cells were used for analysis.

Immunofluorescence

NPCs and iPSC-derived astrocytes were plated at 45,000 cells/well and iPSCs were plated as colonies on Matrigel (0.08 mg/mL)-coated 8-well glass chamber slides. 24 h post-plating, cell media was aspirated and cells were washed 3×with PBS. Cells were then fixed with 4% paraformaldehyde (10 min, 22 °C), washed 3×with PBS and permeabilised with 0.1% TritonX-100 (10 min, 22 °C). At day 24 of the microglia differentiation, iPSC-derived microglia were plated on Matrigel-coated 8-well glass chamber slides at 100,000 cells/well in STEMdiff Microglia Maturation Media. After microglia maturation for 8 days, media was removed without washing then cells fixed with 4% paraformaldehyde (10 min, 22 °C), washed 3×with PBS and permeabilised with 0.1% TritonX-100 (10 min, 22 °C). Blocking for all cell types was done in 5% (v/v) fetal bovine serum in PBS (blocking solution; 1 h, 22 °C). Primary antibodies were diluted in blocking solution and incubated overnight (4 °C). The following day, cells were washed 3×with PBS and incubated with the appropriate Alexa 488/594-conjugated secondary antibody in blocking solution (1 h, 22 °C) (antibody details and dilutions are shown in Additional file 1: Tables S1 and S2). Cells were washed 3×in PBS and mounted on a glass coverslip in fluroshield with DAPI (Sigma-Aldrich). Confocal microscopy was performed using the LSM800 (Zeiss, ZEN Blue software) and images processed using FIJI image analysis software.

Astrocyte morphology and fluorescent intensity analysis

After cells were fixed and stained as above, imaging and analysis followed Jones et al., [24]. To ensure consistent imaging between samples, the mono-directional scan speed, laser power, digital gain, offset and pinhole (set to 1 airy unit) were kept constant for all experiments. Images were taken as 34 z-sections spaced at 0.47 µm intervals on a 10×air objective and processed as maximum intensity projections in FIJI. A minimum of 80 cells were imaged from 2 random fields for each cell line. Morphological analysis of astrocytes was carried out by visually binning each cell into one of three categories defined by Jones et al. [24]: arborised (defined as having greater than 2 distinct processes where the longest extended further than the width of the cell body), bipolar (defined as having 2 distinct processes where the longest extended further than the width of the cell body) and process devoid (defined as having the longest process extended less than the width of the cell body). Cell perimeter,

area, GFAP/S100β fluorescent intensity and circularity was calculated using FIJI. Circularity was defined as $4*\pi*Area/Perimeter^2$, with a value of 1 describing a perfectly circular object. Cell volume was calculated using the z-stack described above and calculated using the '3D object counter' plugin within FIJI.

Microglia morphology analysis

iPSC-derived microglia-like cells were fixed and stained for the marker IBA1 and confocal microscopy was performed using the LSM800 (Zeiss, ZEN Blue software). Image processing and morphological quantification was conducted in FIJI and followed the protocol previously developed by Young and Morrison (2018). A minimum of 80 cells were imaged and analysed in duplicate for each cell line. IBA1 images were converted to grayscale and edge features were enhanced by applying an unsharp mask (pixel radius: 3 and mask weight: 0.6). Individual pixel background noise was removed through the 'despeckle' function. Images were then manually thresholded to a value that included processes without background signal to create a binary image. Background noise was then removed using the 'despeckle' function and pixels less than 2 pixels apart joined using the 'close' function. Bright pixel outliers were removed through the 'remove outliers' function (pixel radius: 2 and threshold: 50). The process binary images were then automatically skeletonised and analysed using the 'analyse skeleton' function. Measurements that contained < 2 branches were background noise and removed from the analysis.

$A\beta_{42}$ production and purification

Overexpression and purification of unlabeled $A\beta_{42}$ was performed according to Walsh et al. [32]. Briefly, large cultures of *Escherichia coli* BL21 Gold (DE3) were incubated at 37 °C with shaking, induced with 0.5 mM isopropyl β-D-1-thiogalactopyranoside and harvested by centrifugation. Purification involved a series of sonication and centrifugation steps followed by resuspension of inclusion bodies in 8 M urea. Anion exchange chromatography using diethylaminoethyl cellulose beads was performed and protein eluted with 150 mM NaCl. $A\beta_{42}$ elution was assessed by electrophoresis, using Novex 10–20% Tricine SDS-PAGE gels. Fractions containing high levels of protein were combined and aliquoted, and lyophilised. A single aliquot was resuspended in 6 M GuHCl 20 mM NaH_2PO_4 pH 8.0 and filtered through a 30-kDa molecular mass cut-off centrifugal filtration device (Amicon Ultra-15) and kept at room temperature for 1 h. A Sephadex G-25 column was equilibrated with 50 mM ammonium acetate pH 8.5 and protein sample loaded onto the beads. Fractions were collected in Protein LoBind Eppendorf and immediately placed on ice. $A\beta_{42}$ elution was assessed by electrophoresis, using Novex 10–20% Tricine SDS-PAGE gels and aliquots were snap-frozen in liquid nitrogen and lyophilised. Freeze-dried protein was resuspended in hexafluoro-2-propanol at 1 mg/ml and incubated for 30 min at RT. Protein was snap-frozen, lyophilised, and stored at − 80 °C until use. Lyophilised protein was gently resuspended in 10 mM NaOH at 2 mg/mL and bath sonicated in ice water for 1 min. 20 mM NaH_2PO_4 pH 6.6 was added at 1:2 ratio v/v (NaOH: NaH_2PO_4). The sample was centrifuged at 16,000 × *g* for 10 min at 4 °C. Concentration was measured using $\varepsilon 275 = 1450\ M^{-1}\ cm^{-1}$ and protein was maintained on ice until use.

IL-6 cytokine ELISA

iPSC-derived astrocytes were plated on Matrigel-coated (0.08 mg/well) 96-well plates at a density of 40,000 cells/well in astrocyte media. 24 h after plating, media was aspirated and cells were exposed to 10 or 50 µg/mL lipopolysaccharide (LPS) (*E. coli* strain 0111:B4; Sigma-Aldrich) (MilliQ H_2O vehicle) or to 5 or 10 µM $A\beta_{42}$ in astrocyte media for 24 h. Media was removed, centrifuged (10,000 g, 1 min) and the supernatant stored at − 80 °C. IL-6 ELISA was performed according to the manufacturer's protocol (R&D Systems product number DY206), with slight amendments including: capture antibody used at 2 µg/mL, detection antibody used at 50 ng/mL and standard range used from 0.586–600 pg/mL. Absorbance at 450 nm was recorded using a BMG POLARstar Omega and analysed using a sigmoidal dose–response (variable slope) model, with unknowns interpolated in GraphPad Prism 9.

PCR and Sanger sequencing

iPSCs were grown to 80% confluency on Matrigel-coated 6-well plates. Genomic DNA was extracted using the Purelink Genomic DNA Mini Kit (Invitrogen), and concentration and purity was determined using the Nanodrop ND-1000 Spectrophotometer. The APOE region was amplified using PCR, where 500 ng DNA was mixed with 25 uL NEB Next High-Fidelity 2X PCR Master Mix, 500 nM forward primer (TCTTGGGTCTCTCTGGCTCA; Integrated DNA Technologies), and 500 nM reverse primer (GCTGCCCATCTCCTCCATC; Integrated DNA Technologies). The reaction was amplified using a T100 thermal cycler (Bio-Rad), with the following program: initial denaturation at 98 °C for 30 s, followed by 40 cycles of denaturation for 10 s at 98 °C, annealing for 15 s at 69 °C and extension for 30 s at 72 °C; then a final extension at 72 °C for 2 min. Electrophoresis was performed on an E-gel Powerbase V4 (Invitrogen) at 100 V for 30 min, using a 1.2% agarose E-Gel with SYBR Safe (Invitrogen), then visualised using an E-Gel Safe Imager

Real Time Transilluminator (Invitrogen) to ensure specific amplification. The product band was excised from the gel, and purified using the QIAquick Gel Extraction Kit (Qiagen). The purified PCR product was then submitted to AGRF for Sanger sequencing, and sequences at SNP locations rs429358 and rs7412 were analysed using SnapGene version 6.1.1.

Multi-cytokine arrays

iPSC-derived astrocytes were plated on Matrigel-coated (0.08 mg/well) 12-well plates at a density of 407,000 cells/well in 1.1 mL/well astrocyte media. 48 h after plating, cell supernatants were removed, centrifuged (10,000*g*, 1 min) and the resulting supernatants stored at − 80 °C until analysed. At day 24 of the microglia differentiation, the cells were plated on Matrigel-coated 8-well glass chambers at 100,000 cells/well in STEMdiff Microglia Maturation Media. After microglial maturation for 8 days, media was removed, centrifuged (10,000 g, 1 min) and the supernatant stored at − 80 °C until analysed. In addition to basal conditions, 10 μM monomeric Aβ was added to the cells 24 h prior to the collection of media in both conditions. Protein levels were measured using the Proteome Profiler Human Cytokine Array Kit (R&D Systems product number ARY005B) as per the manufacturer's instruction, using 1 mL and 0.5 mL of astrocyte and microglia supernatant, respectively. Each membrane was imaged using the Chemi-Doc MP system (Bio-rad) at a constant exposure time for all experiments. Signal intensity for each protein was conducted in duplicate and determined through total pixel intensity using FIJI.

$A\beta_{42:40}$ ELISA and BCA

iPSC-derived astrocytes were plated in Matrigel-coated (0.08 mg/well) 96-well plates at a density of 40,000 cells/well in astrocyte media. Conditioned media was collected 72 h after plating and Aβ levels quantified using a human/rat β-amyloid 40 ELISA Kit and-β amyloid 42 ELISA Kit high sensitive (Wako) according to the manufacturer's protocol. The $A\beta_{40}$ and $A\beta_{42}$ standard range ranged from 1 to 100 pmol/L and 1 to 20 pmol/L, respectively. For determination of total protein concentration, astrocytes were washed with PBS, lifted using accutase (5 min, 37 °C, 5% CO_2) and centrifuged (300 g, 5 min). Cells were then resuspended in RIPA buffer (Thermo Fisher Scientific) containing 1 × protease inhibitor (Merck). Protein concentration per well was determined by the Pierce™ BCA protein assay (Thermo Fisher Scientific) according to the manufacturer's protocol. Within the BCA assay, the bovine serum albumin protein standard ranged from 25 to 2000 μg/mL. Absorbance at 450 nm was recorded using a BMG POLARstar Omega and analysed using a sigmoidal dose–response (variable-slope) model, with unknowns interpolated in GraphPad Prism 9. Interpolated $A\beta_{42:40}$ concentrations were then normalised to total protein concentration for each condition.

Astrocyte viability analysis

After exposure to 5 or 10 μM monomeric $A\beta_{42}$ for 24 h, astrocyte viability was assessed using the Live/Dead Viability/Cytotoxicity Kit (Molecular Probes) according to manufacturer's instructions. Each condition was represented as a percentage of basal (vehicle-control).

Fluorescent $A\beta_{42}$ phagocytosis assay

iPSC-derived astrocytes were plated on Matrigel-coated (0.08 mg/mL) 8-well glass chambers at a concentration of 25,000 cells/well. Twenty-four hours after plating astrocytes and 8 days after microglial maturation, cells were exposed to 2 μg/mL Fluo-488-labelled $A\beta_{42}$ (Anaspec) and left to phagocytose for 2 h (37 °C, 5% CO_2). Media was removed, cells washed 1 × with PBS, fixed with 4% paraformaldehyde (10 min, RT) then washed a further 3×. Cells were imaged on the Cytation 3 Cell Imaging Multi-Mode Reader (BioTek, Gen5 v2 software) under a 10 × air objective, ensuring a constant exposure time and laser intensity across experiments.

Statistical analysis

All data are presented as the mean ± SD of three cell lines with $n \geq 2$ independent experiments per line. Observers were blinded during the collection and analysis of all data. Data were analysed using a one-way ANOVA with Tukey's multiple comparison test or by an unpaired t-test with the exception of the multi-cytokine array. The multi-cytokine array was analysed using multiple unpaired t-tests with a false discovery rate set to 5%. Cytokines that yielded an average intensity value less than 10% of the maximum were considered not to be above background and not included in the statistical analysis. All data were analysed in GraphPad Prism and significance was shown by $^{*}p < 0.05$, $^{**}p < 0.01$ and $^{***}p < 0.001$.

Results

AD-derived astrocytes and microglia-like cells show no deficits in differentiating from iPSCs

The generation of iPSC-derived astrocytes and microglia-like cells occurred through multiple stages, with an overview of each stage represented in Fig. 1. To generate astrocytes in vitro, iPSCs were first aggregated into embryoid bodies then promoted to a neuroectoderm fate. The generation of a neuroectoderm lineage was evidenced through the production of neural rosettes, presenting as neural tube-like structures. These rosettes were selectively replated, and the resulting NPCs were

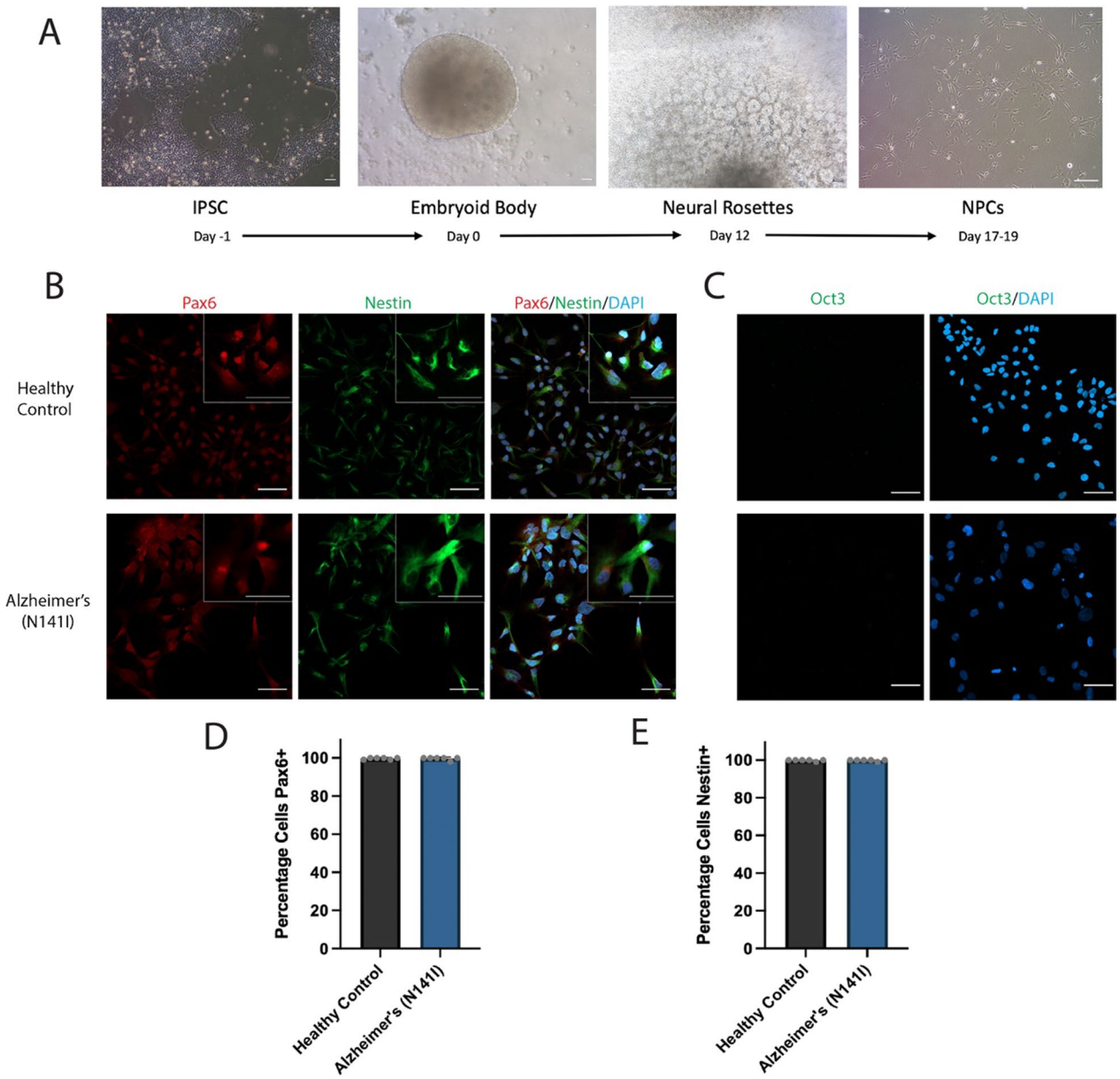

Fig. 1 **A** Overview of differentiation timeline for iPSC-derived NPCs showing representative brightfield images on the last day of each stage. Representative immunofluorescence images of iPSC-derived NPCs from healthy control lines and familial AD lines harbouring a PSEN2 (N141I) mutation. The cells were stained for **B** the neural progenitor markers Pax-6 (red) and Nestin (green), **C** a pluripotency marker Oct3 (green) and all nuclei were counterstained with DAPI (blue). Insert shows higher magnification. All scale bars = 50 µm. The percentage of iPSC-derived NPCs positive for **D** Pax6 and **E** nestin, with each bar displaying the mean ± SD of three cell lines with n ≥ 2 independent experiments per line. Immunofluorescence staining of all iPSC and astrocyte cell lines can be found in Additional file 1: Fig. S2, S3 and S4

expanded for the subsequent few passages (Fig. 1A). The successful generation of NPCs was confirmed through a panel of immunofluorescence markers prior to further differentiation into astrocytes. The cells stained strongly for the NPC markers nestin and Pax6 while being absent for the pluripotency marker Oct3 (Fig. 1B, C). Nestin staining was stronger in the cytoplasm while Pax6 staining was more localised to the nucleus. This pattern is consistent with that in previously reported primary and stem-cell derived NPCs [33]. These results gave us confidence that the cells generated were a pure population of successfully differentiated NPCs and were suitable for further differentiation into astrocytes.

After 4 weeks of further differentiation in astrocyte media, the resulting cells showed positive immunofluorescence staining for the canonical marker GFAP and mature astrocyte marker S100β. Furthermore, the absence of nestin staining confirmed the protocol had successfully transitioned NPCs to a pure population of astrocytes (Fig. 2A, B). The RNA Sequencing (RNASeq) transcriptomic signature of the 3 control iAstrocyte lines derived in this study clustered with that of commercial primary fetal astrocytes grown in our lab and clustered away from neurons and the neural precursor cells used to derive the iAstrocytes (Additional file 1: Fig S5A, B). The iAstrocyte lines only contained 2 differentially expressed genes compared to the commercial fetal astrocytes. This is in contrast to the 1341 genes that were differentially expressed between the iAstrocytes and the NPCs used to derive them (Additional file 1: Fig S5C–E).

We found no significant difference between the Alzheimer's PSEN2 (N141I) lines or healthy controls in the percentage of cells positive for GFAP (97% ± 3.7 SD and 97% ± 1.5 SD, respectively) or S100β (98% ± 3.1% and 98% ± 1.9 SD, respectively) (Fig. 2A–D).

Intermediate filament changes are known to be present within reactive astrocytes [34], as such, we conducted fluorescent intensity analysis of GFAP and S100β to gain an initial insight into the activation profile of AD-derived astrocytes. We observed the fluorescence intensity of GFAP to be significantly elevated in AD-derived astrocytes compared to healthy controls (84.3 a.u ± 26.3 SD

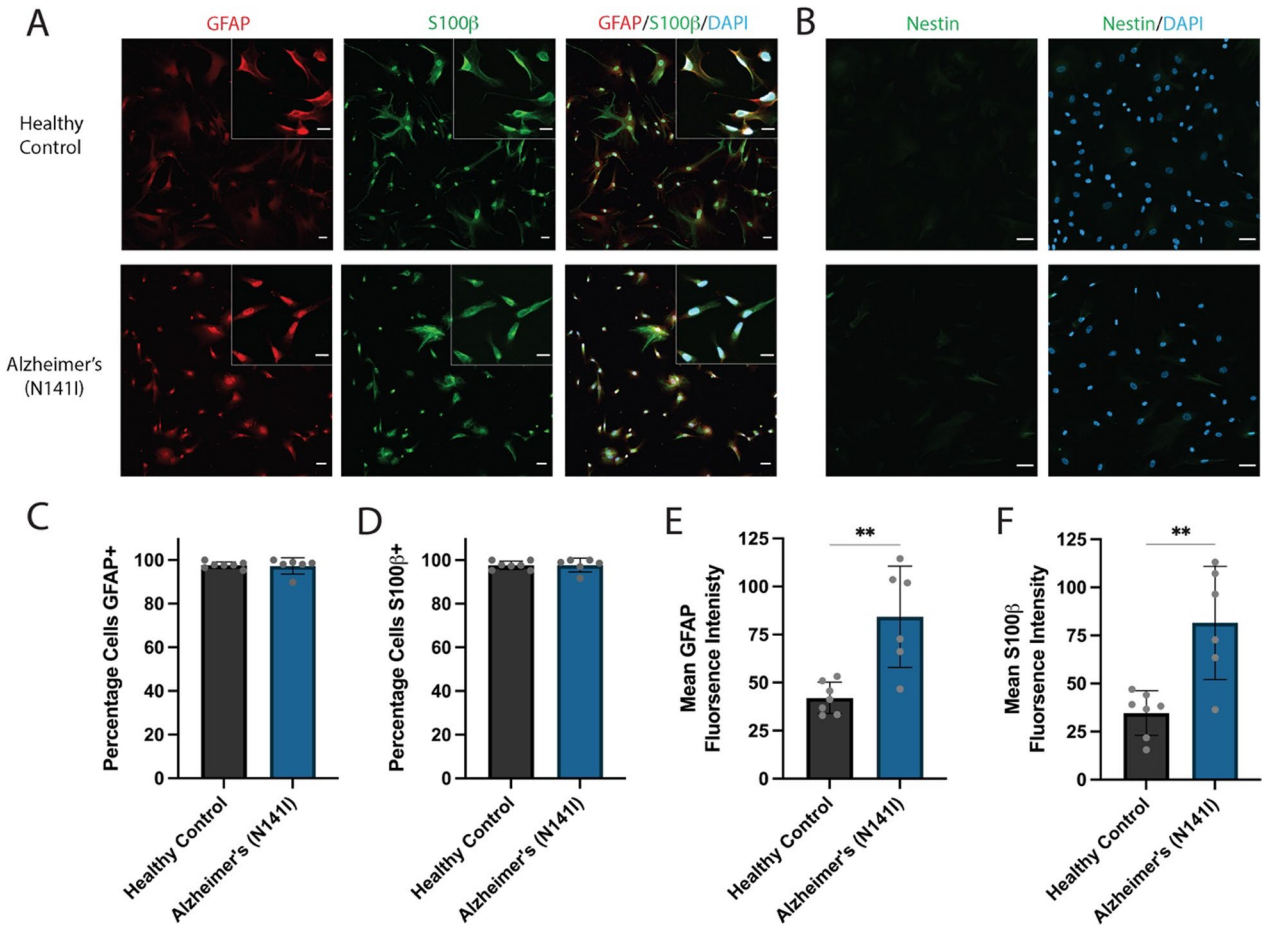

Fig. 2 **A** Representative immunofluorescence images of iPSC-derived astrocytes from healthy control lines and familial AD lines harbouring a PSEN2 (N141I) mutation. The cells were stained for astrocyte markers GFAP (red) and S100β (green) and **B** the NPC marker nestin (green) and all nuclei were counterstained with DAPI (blue). Insert shows higher magnification. All scale bars = 50 µm. The percentage of iPSC-derived astrocytes positive for C) GFAP and **D** S100β. Mean fluorescence intensity of **E** GFAP and **F** S100β per astrocyte. An unpaired t-test was used to test whether there were statistically significant differences between the means of AD-derived and healthy control astrocytes. Each bar displays the mean ± SD of three cell lines with n ≥ 2 independent experiments per line (**$p < 0.01$). Immunofluorescence staining of all cell lines can be found in Additional file 1: Fig. S4

and 42.1 a.u ± 8.19 SD, respectively) ($p < 0.01$; Fig. 2E). A significant increase in S100β intensity from AD-derived astrocytes was also observed relative to healthy controls (81.6 a.u ± 29.4 SD and 34.7 a.u ± 11.6 SD, respectively) ($p < 0.01$; Fig. 2F).

To generate iPSC-derived microglia-like cells, we followed a method based on a previously published protocol

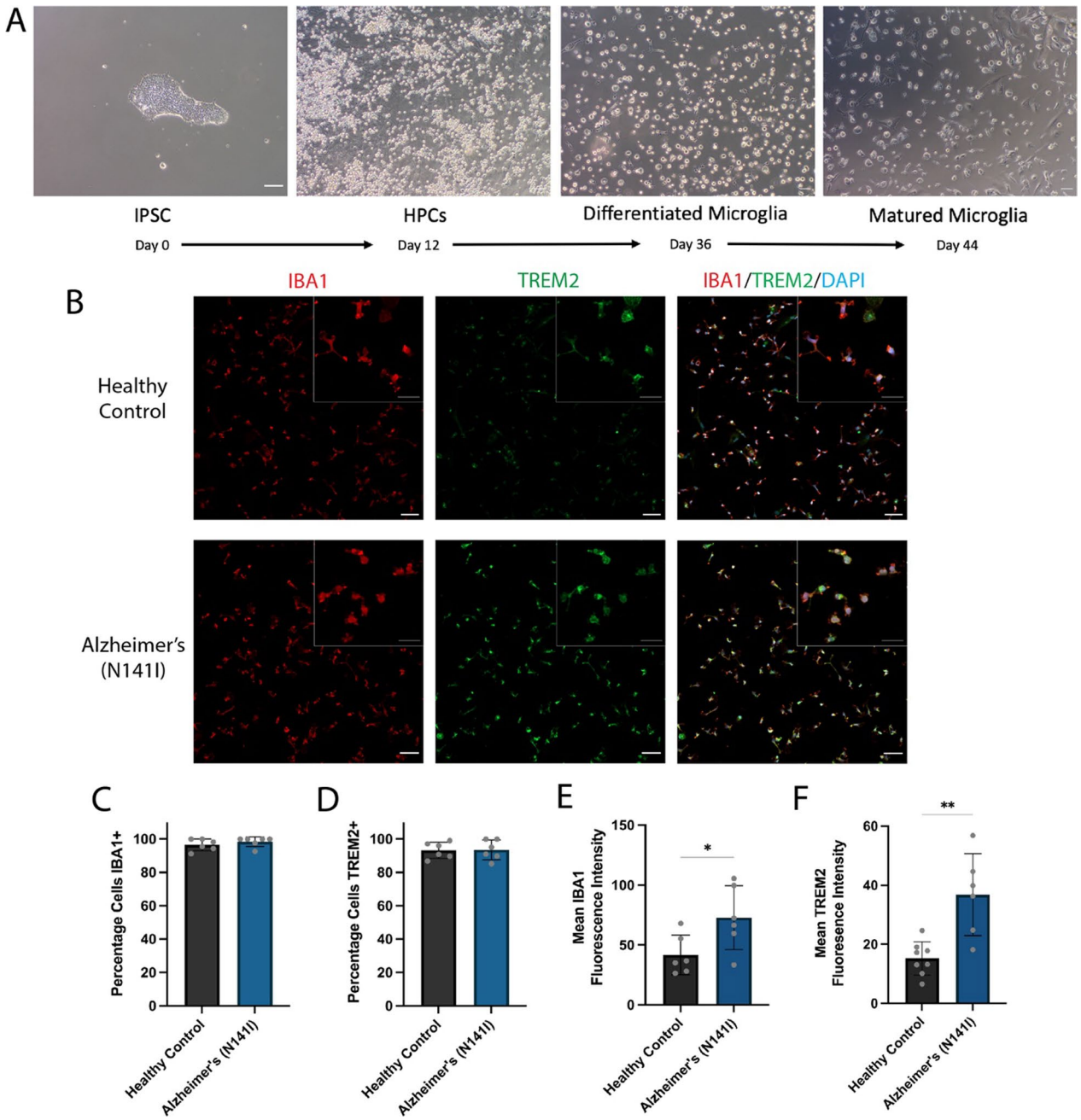

Fig. 3 **A** Overview of differentiation timeline for iPSC-derived microglia-like cells showing representative brightfield images on the last day of each stage. **B** Representative immunofluorescence images of iPSC-derived microglia from healthy control lines and familial AD lines harbouring a PSEN2 (N141I) mutation. The cells were stained for microglial markers IBA1 (red), TREM2 (green) and all nuclei were counterstained with DAPI (blue). Insert shows higher magnification. All scale bars = 50 µm. The percentage of iPSC-derived microglia-like cells positive for **C** IBA1 and **D** TREM2. Mean fluorescence intensity of **E** IBA1 and **F** TREM2 per cell. An unpaired *t*-test was used to test whether there were statistically significant differences between the means of AD-derived and healthy control microglia. Each bar displays the mean ± SD of three cell lines with $n \geq 2$ independent experiments per line (**$p < 0.01$). Immunofluorescence staining of all cell lines can be found in Additional file 1: Fig. S6

which produced microglia-like cells with gene expression profiles and functional activity very similar to those of primary human fetal and adult microglia [22, 35]. In short, iPSCs were plated as small colonies, patterned into floating HPC intermediates and then further differentiated into microglia-like cells (overview shown in Fig. 3A). At the end of the derivation, the microglia-like cells exhibited strong staining for the microglial/monocyte marker IBA1 and microglial-enriched protein TREM2 (Fig. 3B). The percentage of the cell population positive for the two markers was high (> 90%) and did not significantly differ between AD-derived and healthy control lines for IBA1 (98.4% ± 3.0 SD and 96.6% ± 3.5 SD, respectively) or TREM2 (93.5% ± 5.9 SD and 93.3% ± 4.8 SD, respectively) (Fig. 3C, D). Altered expression of IBA1 and TREM2 within microglia play a role in regulating cellular activation and inflammatory cytokine release [36, 37]. Compared to healthy controls, AD-derived microglia-like cells showed a significant increase in the fluorescence intensity of IBA1 (41.7 a.u ± 16.6 SD and 72.9 a.u ± 26.7 SD, respectively) ($p < 0.05$; Fig. 3E) and TREM2 (15.2 a.u ± 5.7 SD and 36.8 a.u ± 13.9 SD, respectively) ($p < 0.01$; Fig. 3F).

The results presented herein reveal that the fAD-causative PSEN2 (N141I) mutation did not affect the ability of iPSCs to successfully differentiate into mature astrocytes or microglia-like cells in vitro, although the expression of the astrocytic proteins GFAP and S100β were shown to be upregulated in PSEN2 (N141I)-mutant astrocytes.

AD-derived astrocyte morphology is atrophied, less heterogenous and more reactive

Previous reports of iPSC-derived astrocytes from both sporadic and fAD patients have shown these cells exhibit substantial changes to the morphological phenotype compared to astrocytes derived from healthy control iPSCs [24]. Hence, we quantified the morphological profiles of iPSC-derived astrocytes from our cohort of fAD patients and healthy controls. AD-derived PSEN2 (N141I)-mutant astrocytes displayed a significant reduction in the average perimeter of each cell compared to healthy controls (142.1 μm^2 ± 47.5 SD and 409.1 μm^2 ± 212.7 SD, respectively) ($p < 0.05$; Fig. 4A). Cellular circularity is a quantitative index reflecting the extent of process extension, with a measurement of 1 describing a perfectly round cell. AD-derived astrocytes exhibited a rounder, more spherical shape in comparison to healthy control astrocytes, as shown by a significant increase in cellular circularity (0.55 ± 0.09 SD and 0.31 ± 0.10 SD, respectively) ($p < 0.001$; Fig. 4B). Three-dimensional reconstruction and determination of cell volume was conducted using fine z-stacks, finding AD-derived astrocytes to have a significant reduction in average cell volume compared to healthy controls (7653 μm^3 ± 2889 SD and 21,126 μm^3 ± 9911 SD, respectively) ($p < 0.01$; Fig. 4C).

To examine how morphological distribution of astrocytes varied across the cellular population, we classified individual astrocytes into various morphological categories. These categories included 'arborised', 'polarised' and 'process devoid' astrocyte morphologies, previously defined by Jones et al. [24]. Healthy control astrocytes most commonly presented as large cells with multiple lengthy, branching processes which is highly characteristic of an archetypal astrocyte morphology, referred to as 'arborised' (47.9% ± 6.7 SD) (Fig. 4D). The remaining cells were similarly split between bipolar-type cells protruding two main processes, referred to as 'polarised' (22.5% ± 4.1 SD), and smaller cells with small to no extensions protruding from the cell body, referred to as 'process devoid' (29.7% ± 10.3 SD) (Fig. 4D). Representative images of each morphological classification are shown in Fig. 4E. In contrast, AD-derived astrocytes showed a general reduction in cellular heterogeneity compared to healthy controls. Specifically, AD astrocytes were predominantly comprised of process-devoid cells (72.3% ± 14.9 SD), which constituted a significantly higher proportion of cells compared to healthy controls ($p < 0.001$; Fig. 4D). The proportion of AD-derived astrocytes that exhibited the archetypal arborised morphology was significantly lower than healthy controls (14.2% ± 12.1 SD) ($p < 0.001$; Fig. 4D), however there was no significant difference between the proportion of polarised cells (Fig. 4D).

AD-derived microglia show less complex ramification

Reduction in the extent and complexity of microglial ramification isolated from the post-mortem brain tissue of AD patients has been previously reported [38, 39]. These changes in morphological structure are hypothesised to parallel changes in AD-associated microglial functions. Hence, we performed a quantitative analysis of iPSC-derived microglial-like cell morphology and characterised cellular ramifications through the number, length and complexity of branching processes. The automated analysis of immunofluorescence images presented herein closely followed a previously developed protocol [40]. A representative image post-processing and skeletonisation is shown in Fig. 5A. AD-derived microglia-like cells showed a significant reduction in the average number of extension branch points, termed junctions, compared to healthy controls (5.9 ± 1.2 SD and 13.4 ± 7.8 SD, respectively) ($p < 0.05$, Fig. 5B). Similarly, AD-derived microglia-like cells showed a significant decrease in the average number of branches compared to healthy controls (12.5 ± 2.6

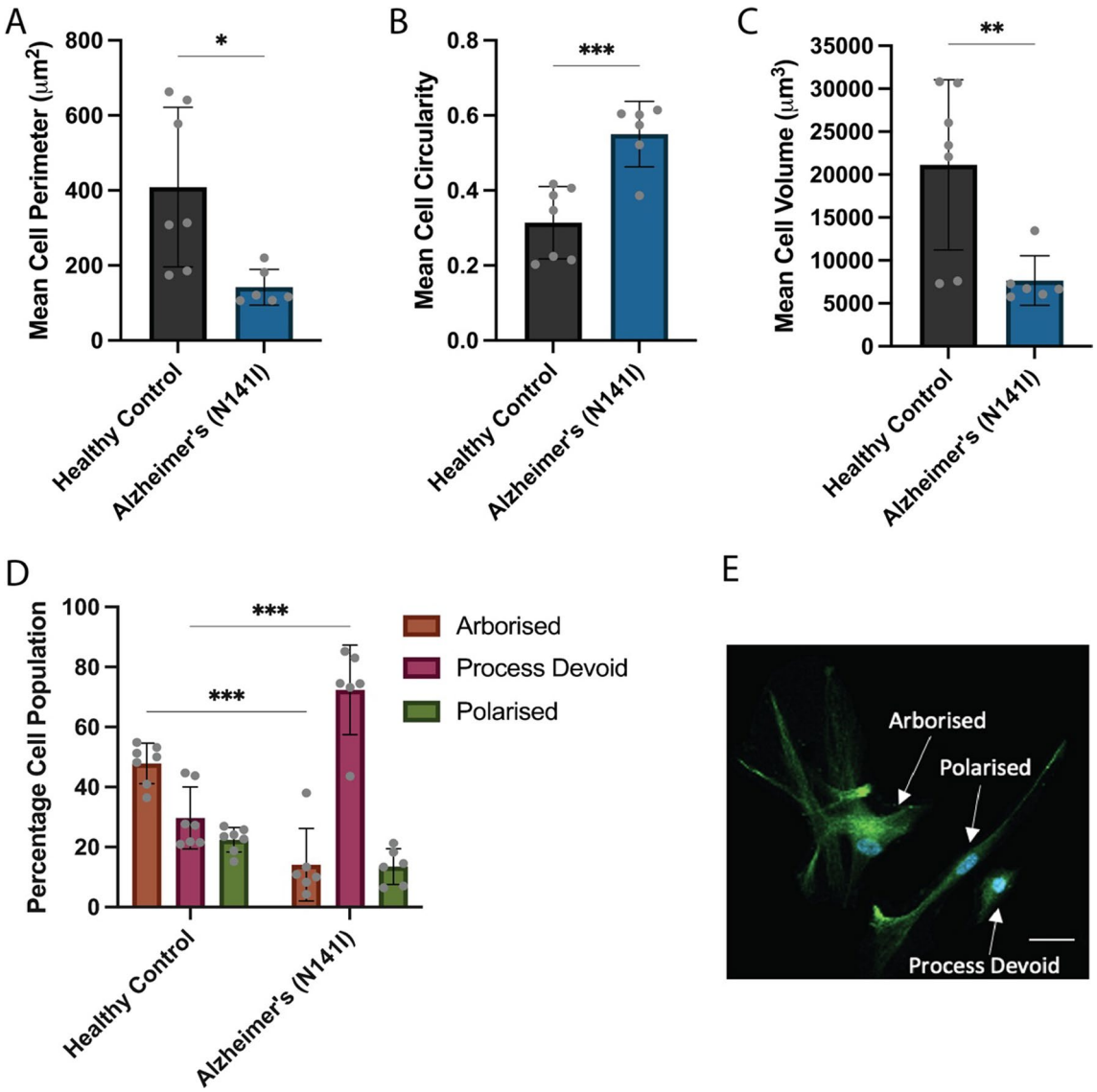

Fig. 4 Morphological characterisation of iPSC-derived astrocytes from three healthy control and three familial AD lines harbouring a PSEN2 (N141I) mutation. Quantification of **A** average cell perimeter, **B** average cell circularity and **C** average cell volume were determined using GFAP and S100β immunofluorescence and 3D reconstruction within FIJI. **D** Individual cells were categorised and based on morphological appearance, with representative phenotypes of 'arborised', 'polarised' and 'process devoid' cells illustrated in **E**. An unpaired *t*-test (**A**–**C**) or two-way ANOVA with a post hoc Dunnett's test (**D**) were used to test whether there were statistically significant differences between the means of AD-derived and healthy control astrocytes for each morphological category. The figure displays the mean ± SD of three cell lines with $n \geq 2$ independent experiments per line (*$p < 0.05$, **$p < 0.01$, ***$p < 0.001$). Scale bar = 50 µm

SD and 25.9 ± 13.8 SD, respectively) ($p < 0.05$, Fig. 5C). Another key metric of ramification includes the number of contact points at the end of each branch, termed endpoints. We found AD-derived microglia-like cells to have significantly fewer endpoints per cell compared to healthy controls (6.8 ± 1.4 and 11.0 ± 3.6 SD, respectively) ($p < 0.05$, Fig. 5D). To gauge how far microglial processes extended from the cell body we analysed the average longest branch length per cell and found no significant difference between AD-derived microglia-like cells and healthy controls (11.6 µm ± 1.9 SD and 13.3 µm ± 4.7 SD, respectively) (Fig. 5E). Taken together, these results demonstrate that PSEN2 (N141I)-mutant astrocytes and microglia-like cells show less complex ramified morphology.

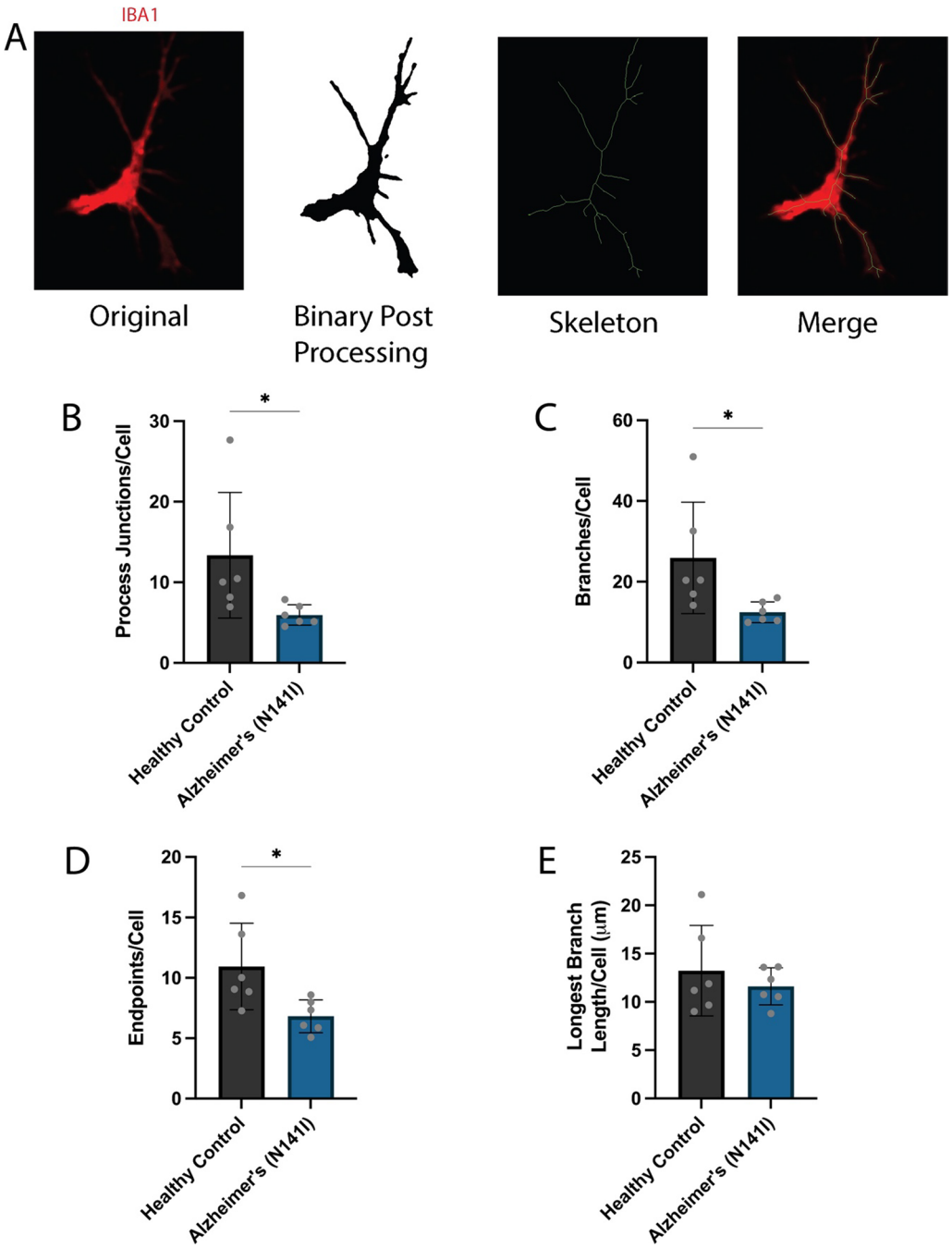

Fig. 5 **A** An example of the processing of an immunofluorescence image of iPSC-derived microglia-like cells stained for IBA1 (red), the result of image processing is shown in binary and was followed by skeletonisation (green). An overlay of the original IBA1 image (red) and skeleton (green) is shown for comparison. Automated analysis of the mean number of **B** junctions, **C** branches, **D** endpoints and **E** longest branch length per cell. An unpaired t-test was used to test whether there were statistically significant differences between the means of AD-derived and healthy control microglia-like cells. The figure displays the mean ± SD of three cell lines with $n = 2$ independent experiments per line (*$p < 0.05$)

AD-derived astrocytes and microglia exhibit an exaggerated pro-inflammatory response to immune challenge

We next aimed to functionally characterise these microglia-like cells and astrocytes in terms of cytokine and chemokine secretion. Firstly, we wanted to confirm that our iPSC-derived astrocytes would respond to LPS stimulation and release IL-6, a signature that

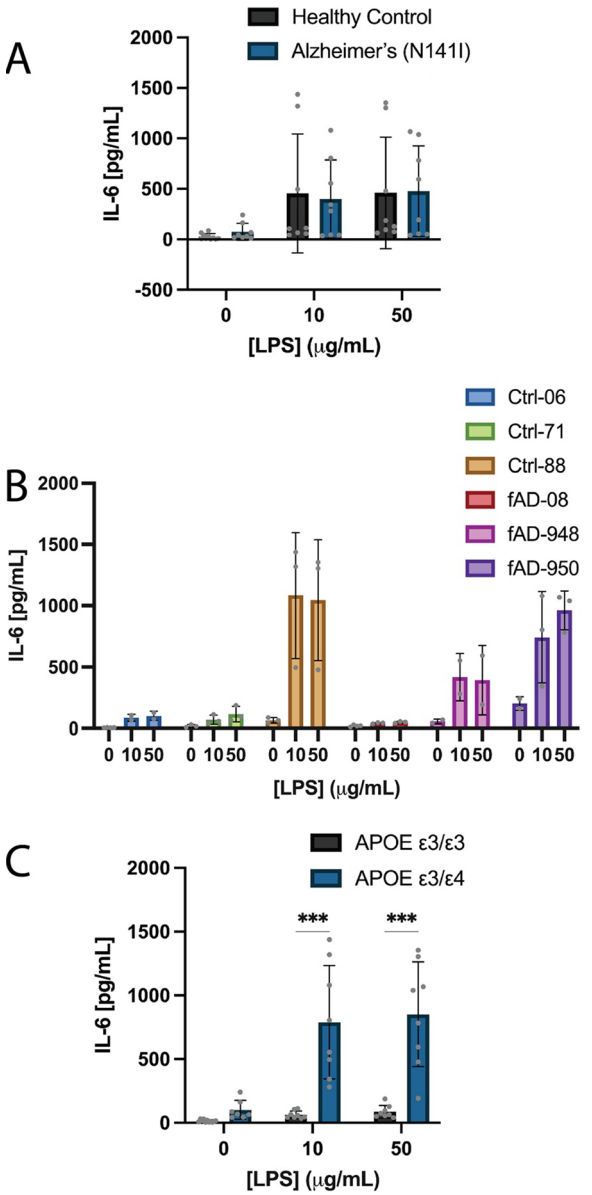

Fig. 6 Concentration of IL-6 secreted from healthy control or AD-derived astrocytes **A** basally and after exposure to 10 or 50 µg/mL LPS for 24 h. **B** Data from part A represented as individual cell lines. Cell lines were re-categorised based on their APOE ε3/ε3 (Ctrl-06, Ctrl-71 and fAD-08) or APOE ε3/ε4 (Ctrl-88, fAD-948 and fAD-950) genotype and shows the concentration of IL-6 secretion **C** basally and after exposure to 10 or 50 µg/mL LPS for 24 h. A two-way ANOVA with multiple comparisons and post hoc Dunnett's test was used to test whether there were statistically significant differences between the means of AD-derived and healthy control astrocytes or APOE ε3/ε3 and APOE ε3/ε4 astrocytes (***$p < 0.001$). Statistical tests were not conducted for figure **B**. Figures **A** and **C** display the mean ± SD of three cell lines with $n \geq 2$ independent experiments per line, B display the mean ± SD of $n \geq 2$ independent experiments per line

we would expect to see from mature astrocytes. Both the healthy control and AD-derived astrocytes basally secreted small amounts of IL-6 (26.9 pg/mL ± 29.4 SD and 74.1 pg/mL ± 83.5 SD, respectively) (Fig. 6A) and showed increased secretion of IL-6 from basal upon stimulation with 10 µg/mL LPS (454.5 pg/mL ± 589.3 SD and 398.3 pg/mL ± 387.7 SD, respectively) and 50 µg/mL LPS (460.6 pg/mL ± 552.3 SD and 478.0 pg/mL ± 447.4 SD, respectively), albeit no significant differences being found between healthy controls and AD-derived astrocytes (Fig. 6A).

A large amount of variability was observed in both the healthy control and AD-derived groups in the basal and LPS-stimulated conditions (Fig. 6 A). In an attempt to identify a source of the large variation in IL-6 secretion, we reorganised the grouped results into their individual cell lines. The Ctrl-88, fAD-948 and fAD-950 cell lines secreted higher IL-6 basally and showed, on average, a 9.2-fold higher response to 10 µg/mL LPS and 7.2-fold to 50 µg/mL LPS compared to the Ctrl-06, Ctrl-71 and fAD-08 lines (Fig. 6B). Further investigation of the genotypes of these three high responding lines (Ctrl-88, fAD-948 and fAD-950) revealed they were heterozygous carriers of the APOE ε4 allele, the largest associated risk gene for sAD. Conversely, the three lower responders (Ctrl-06, Ctrl-71 and fAD-08) were homozygous for the APOE ε3 allele (Table 1). This led us to perform a post hoc analysis where we recategorised cell lines into their respective APOE genotype, being ε3/ε3 or ε3/ε4. We found a non-significant increase in basal IL-6 (ε3/ε3: 13.8 pg/mL ± 9.9 SD and ε3/ε4: 101.4 pg/mL ± 73.7 SD) (Fig. 6C) and significant increases in 10 µg/mL LPS-stimulated (ε3/ε3: 63.6 pg/mL ± 29.4 SD and ε3/ε4: 789.2 ± 444.6 SD) ($p < 0.001$; Fig. 6C) and 50 µg/mL LPS-stimulated IL-6 secretion (ε3/ε3: 87.1 pg/mL ± 48.9 SD and ε3/ε4: 851.5 ± 411.1 SD) ($p < 0.001$; Fig. 6 C) from APOE ε3/ε4 astrocytes compared to APOE ε3/ε3. It is important to note that the statistical test here is not a bona fide reflection of statistical significance due to the post hoc nature of the analysis. Nevertheless, it does provide a hypothesis to explain the variability originally observed when comparing IL-6 secretion from healthy control and AD-derived astrocytes. Furthermore, it provided an important consideration when interpreting results from subsequent IL-6 ELISAs.

In addition to exhibiting neurotoxic properties, $A\beta_{42}$ is known to induce reactive changes in glial states and causes release of pro-inflammatory cytokines [41]. As such, we aimed to test the effect that an AD-relevant stimulus has on our iPSC-derived astrocytes and microglia-like cells. We first characterised the IL-6 response from iPSC-derived astrocytes after being exposed to both 5 and 10 µM monomeric $A\beta_{42}$. AD-derived astrocytes

showed a significantly elevated secretion of IL-6 compared to healthy controls after exposure to both 5 μM (963.2 ± 697.6 SD and 130.0 ± 85.9 SD, respectively) ($p < 0.01$) and 10 μM $A\beta_{42}$ (1023.0 pg/mL ± 621.7 SD and 118.8 pg/mL ± 90.9 SD, respectively) ($p < 0.001$; Fig. 7A). As $A\beta_{42}$ has been shown to be neurotoxic in in vitro cultures of both primary and iPSC-derived neurons [42, 43], we aimed to test whether this toxicity extended to iPSC-derived astrocytes. Neither healthy control or AD-derived astrocytes showed any reduction in cell viability from basal after 5 μM (110.9% ± 15.7 SD and 104.2% ± 3.9 SD, respectively) or 10 μM $A\beta_{42}$ exposure (108.0% ± 24.0 SD and 107.3% ± 18.9 SD, respectively) (Fig. 7B). This provided confidence that the secreted IL-6 was a cellular response and not an artefactual release from apoptotic cells. In light of the previous results found with LPS-stimulated IL-6 secretion and APOE genotype, we conducted a similar post-hoc analysis recategorising the cells into their respective APOE ε3/ε3 and APOE ε3/ε4 genotypes. In contrast to LPS stimulation, we observed a larger amount of variation after reorganisation and no significant differences between the APOE genotypes in IL-6 secretion (Fig. 7C) or cell viability (Fig. 7D) were found after stimulation with 5 or 10 μM $A\beta_{42}$.

After observing significant differences in the release of IL-6 between AD-derived and healthy control-derived astrocytes, we conducted a broader characterisation of cytokines/chemokines from iPSC-derived astrocytes and microglia-like cells using a multi-cytokine array consisting of 36 cytokines/chemokines (Additional file 1: Fig. S7). We observed no significant changes in the basal secretion of cytokines between healthy and AD-derived astrocytes (Fig. 8A). Upon stimulation with 10 μM $A\beta_{42}$ we observed significant increases in the secretion of chemokine (C-X-C motif) ligand 1 (CXCL1) (2974 a.u ± 2677 SD and 10,772 a.u ± 1156 SD, healthy control and AD-derived, respectively) ($p < 0.01$), intercellular adhesion molecule 1 (ICAM-1) (871 a.u ± 185 SD and 4533 a.u ± 1675 SD, healthy control and AD-derived, respectively) ($p < 0.01$), IL-6 (968 a.u ± 426 SD and 5297 a.u ± 4814 SD, healthy control and AD-derived, respectively) ($p < 0.01$) and IL-8 (5297 a.u ± 4814 SD and 21,540 a.u ± 4946 SD, healthy control and AD-derived, respectively) ($p < 0.01$) from the AD-derived astrocytes compared to healthy controls (Fig. 8B). The significant increase in IL-6 mirrors that of the specific IL-6 ELISA previously presented (Fig. 7A) and provides confidence that this lower sensitive multi-cytokine array was detecting differences in moderately low cytokine concentrations.

iPSC-derived microglia-like cells from AD origin showed a significant reduction in the basal secretion of IL-8 compared to healthy controls (26,457 a.u ± 11,408 SD and 3148 a.u ± 2582 SD, respectively) ($p < 0.01$; Fig. 8 C). Upon stimulation with $A\beta_{42}$, AD-derived microglia-like cells showed a considerable increase in IL-8 (12.4-fold from basal), whereas the IL-8 secreted from healthy control microglia-like cells stayed relatively unchanged (1.1-fold decrease) (Fig. 8D). Significantly increased secretion of IL-18 (1473 a.u ± 352 SD and 4299 a.u ± 2006 SD, healthy control and AD-derived, respectively) ($p < 0.05$) and macrophage migration inhibitory factor (MIF) (5483 a.u ± 1635 SD and 12,535 a.u ± 4742 SD, healthy control and AD-derived, respectively) ($p < 0.01$) were observed from AD-derived microglia-like cells compared to healthy controls after $A\beta_{42}$ stimulation (Fig. 8D). We observed a substantial increase in macrophage inflammatory protein-1 (MIP-1) secretion after $A\beta_{42}$ exposure for both the healthy control (27.1-fold increase from basal) and AD-derived microglia-like cells (44.5-fold increase from basal), however there were no significant differences between the final levels of secretion between AD-derived and healthy control microglia-like cells.

In addition to the release of cytokine/chemokines, astrocytes not only secrete Aβ, but are suggested to do so in a high enough quantity to contribute to Aβ load within the brain [44]. Despite this, the effect of fAD-causative mutations on $A\beta_{42}$ production has been primarily studied in neurons. Therefore, we analysed the secretion of the AD-associated peptides $A\beta_{42}$ and $A\beta_{40}$ 72 h post-plating of our control and AD-derived astrocytes harbouring a PSEN2 (N141I) mutation. AD-derived astrocytes produced a significant increase in the secretion of $A\beta_{42}$ compared to healthy controls (0.0600 pg/μg ± 0.0129 SD and 0.0372 pg/μg ± 0.0207 SD, respectively) ($p < 0.05$; Fig. 9A). No significant differences were observed in the secretion of $A\beta_{40}$ (0.317 pg/μg ± 0.076 SD and 0.276 pg/μg ± 0.111 SD, AD-derived and healthy control, respectively) (Fig. 9

(See figure on next page.)

Fig. 7 The concentration of **A** secreted IL-6 and **B** viability of AD-derived and healthy control astrocytes after stimulation with initially monomeric 0, 5 or 10 μM $A\beta_{42}$ for 24 h. Cell lines were re-categorised based on their APOE ε3/ε3 (Ctrl-06, Ctrl-71 and fAD-08) or APOE ε3/ε4 (Ctrl-88, fAD-948 and fAD-950) genotype and shows the concentration of **C** secreted IL-6 and **D** viability after exposure to 0, 5 or 10 μM $A\beta_{42}$ for 24 h. The figure displays the mean ± SD of three cell lines with n ≥ 2 independent experiments per line. A two-way ANOVA with post hoc Dunnett's test was used to test whether there were statistically significant differences between mean of AD-derived and healthy control astrocytes and APOE ε3/ε3 and APOE ε3/ε4 astrocytes (**$p < 0.01$, ***$p < 0.001$)

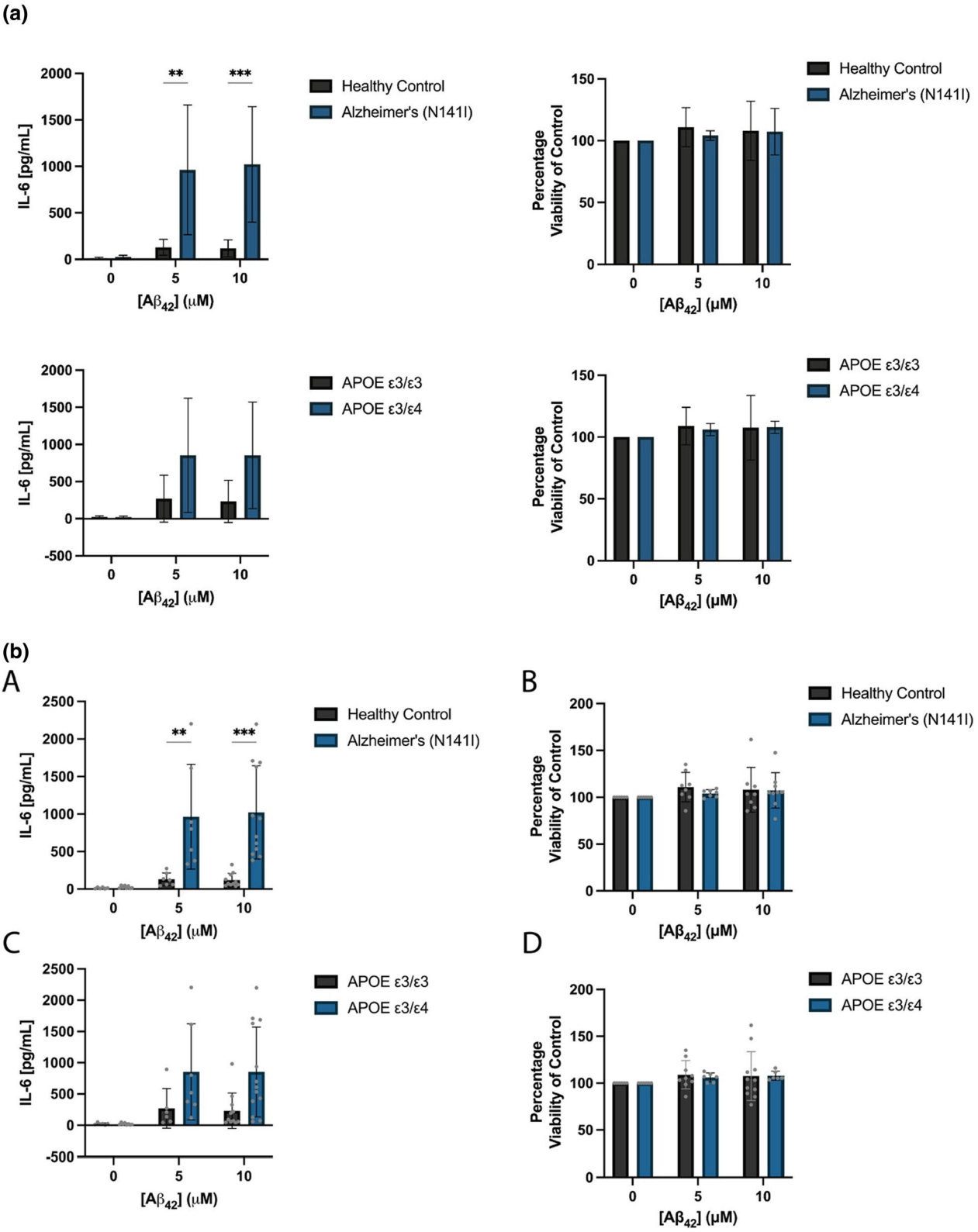

Fig. 7 (See legend on previous page.)

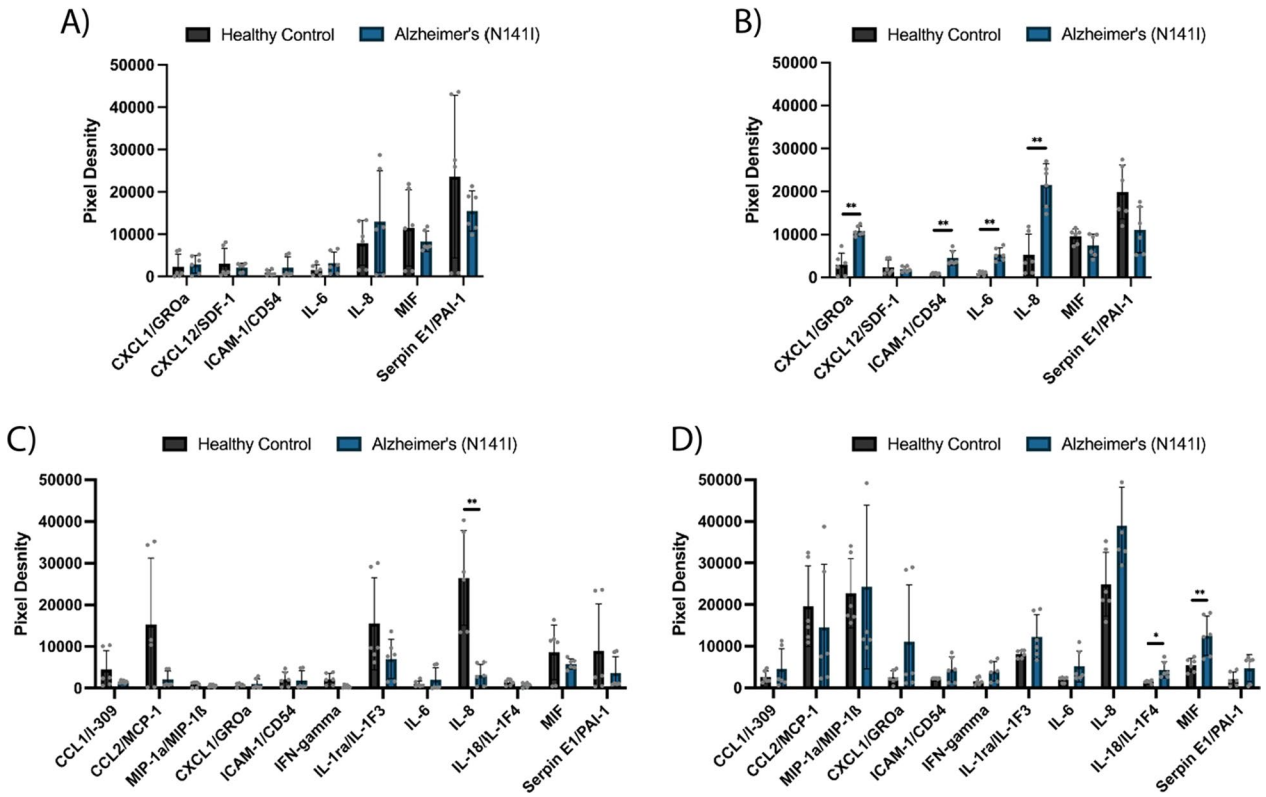

Fig. 8 Multi-cytokine array of AD-derived or healthy iPSC-derived astrocytes **A** basally and **B** after 24 h exposure to 10 μM $A\beta_{42}$ and iPSC-derived microglia-like cells **C** basally and **D** after 24 h exposure to 10 μM $A\beta_{42}$. The figure displays the mean ± SD of three cell lines with the average of two experimental duplicates per line. Multiple unpaired, non-parametric Mann–Whitney *t*-tests adjusting for a 5% false discovery rate were used to test whether there were statistically significant differences between mean cytokine/chemokine release of AD-derived and healthy control astrocytes and microglia-like cells (*$p < 0.05$, **$p < 0.01$). Cytokines/chemokines with mean pixel density under 10% of the maximum in both basal and $A\beta_{42}$-stimulated conditions were considered background and are not shown, full cytokine array is shown in Additional file 1: Figs. S7 and S8

B), the ratio of $A\beta_{42:40}$ (0.177 ± 0.068 SD and 0.127 ± 0.023 SD, AD-derived and healthy control, respectively) (Fig. 9C) or total level of Aβ secreted (0.362 pg/μg ± 0.079 SD and 0.322 pg/μg ± 0.144 SD, AD-derived and healthy control, respectively) (Fig. 9D) between AD-derived astrocytes and healthy controls. Additionally, we found no differences in the levels of $A\beta_{42}$, $A\beta_{40}$, the $A\beta_{42:40}$ ratio and total Aβ between APOE ε3/ε3 and APOE ε3/ε4 astrocytes (Additional file 1: Fig. S9).

Astrocyte and microglial phagocytosis of $A\beta_{42}$

Phagocytosis is one of the major functions of CNS glial cells. To assess the phagocytic capacity of AD-derived and healthy control astrocytes and microglia-like cells, we exposed the glial cells to fluorescently tagged fibrillar $A\beta_{42}$ based on a previously published protocol using iPSC-derived microglia [45]. AD-derived astrocytes on average exhibited significantly greater uptake of fluorescent $A\beta_{42}$ fibrils per cell compared to healthy controls ($1.33 \times 10^7 \pm 8.67 \times 10^6$ SD and $3.84 \times 10^6 \pm 3.62 \times 10^6$ SD, respectively) ($p < 0.05$; Fig. 10A). The proportion of astrocytes that showed $A\beta_{42}$ uptake was very high (> 95%) in both the AD-derived and healthy control lines, finding no statistical differences between each group (98.7% ± 1.5 SD and 97.4% ± 3.3 SD, respectively) (Fig. 10B). Similarly, iPSC-derived microglia-like cells showed a very high proportion of phagocytic cells (> 95%) with no significant differences between AD-derived and healthy controls (97.5% ± 2.2 SD and 98.5% ± 0.9 SD, respectively) (Fig. 10D). Surprisingly, we observed no significant differences between the amount of $A\beta_{42}$ taken up by AD-derived or healthy control microglia-like cells ($2.71 \times 10^6 \pm 1.30 \times 10^6$ SD and $1.64 \times 10^6 \pm 1.15 \times 10^6$ SD, respectively) (Fig. 10C). Representative images of iPSC-derived astrocytes (Fig. 10E) and microglia-like cells (Fig. 10F) showcases the strong uptake of fluorescent $A\beta_{42}$ and high proportion of phagocytic cells.

Discussion

Astrocytes and microglia play a crucial role in many aspects of AD pathophysiology such as release of pro-inflammatory cytokines and dysregulation of Aβ

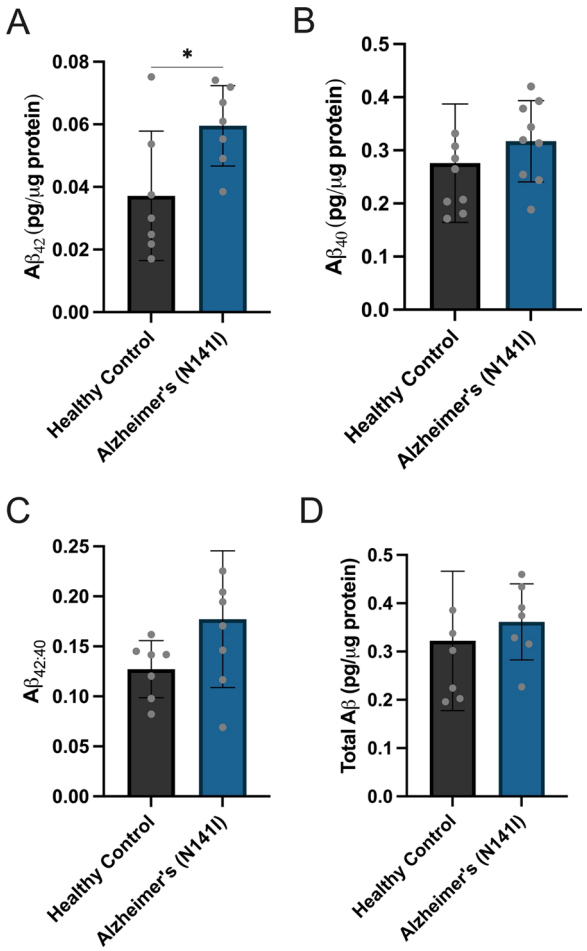

Fig. 9 Concentrations of **A** $A\beta_{42}$, **B** $A\beta_{40}$, **C** the ratio of $A\beta_{42:40}$ and **D** total Aβ protein quantified from iPSC-derived astrocyte supernatants 72 h after plating. Secreted Aβ concentrations were measured using a highly sensitive ELISA and normalised to total protein concentration determined by BCA. The figure displays the mean ± SD of three cell lines with $n \geq 2$ independent experiments per line. An unpaired t-test was used to test whether there were statistically significant differences between mean of AD-derived and healthy control astrocytes (*$p < 0.05$)

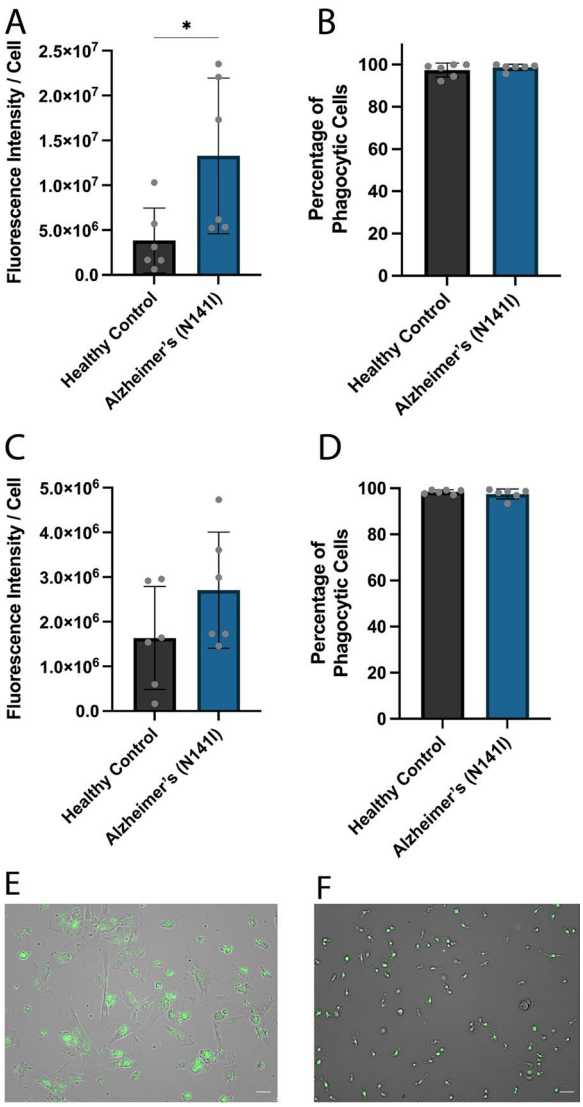

Fig. 10 AD-derived and healthy **A** iPSC-derived astrocytes and **B** iPSC-derived microglia-like cells were exposed to 488-fluorescent-$A\beta_{42}$ fibrils for 2 h and phagocytosis was quantified through average fluorescent intensity per cell. The figure shows the percentage of **B** iPSC-derived astrocytes and **D** iPSC-derived microglia-like cells which show any uptake of $A\beta_{42}$. The figure displays the mean ± SD of three cell lines with n ≥ 2 independent experiments per line. An unpaired t-test was used to test whether there were statistically significant differences between mean of AD-derived and healthy control astrocytes (*$p < 0.05$). Representative overlay of brightfield and fluorescent images of **E** iPSC-derived astrocytes and **F** iPSC-derived microglia-like cells, fluorescent $A\beta_{42}$ fibrils shown in green, scale bar = 50 µm

proteostasis. However, the specific cellular dysfunction occurring and the molecular drivers of glial activation during various stages of AD progression is not well understood. Here, we describe the previously unreported differentiation and characterisation of iPSC-derived astrocytes and microglia-like cells from fAD patients harbouring a PSEN2 (N141I) mutation. We showed that PSEN2 (N141I)-mutant astrocytes and microglia-like cells presented with an extensive disease-associated phenotype with reduced morphological complexity, exaggerated pro-inflammatory cytokine secretion and altered $A\beta_{42}$ production and phagocytosis (summarised in Fig. 11).

It is worthy of note that classifying in vitro iPSC-derived microglia-like cells as bona fide microglia is a somewhat contentious topic within literature and is generally supported with extensive transcriptomic analysis [22]. Despite our differentiation following a

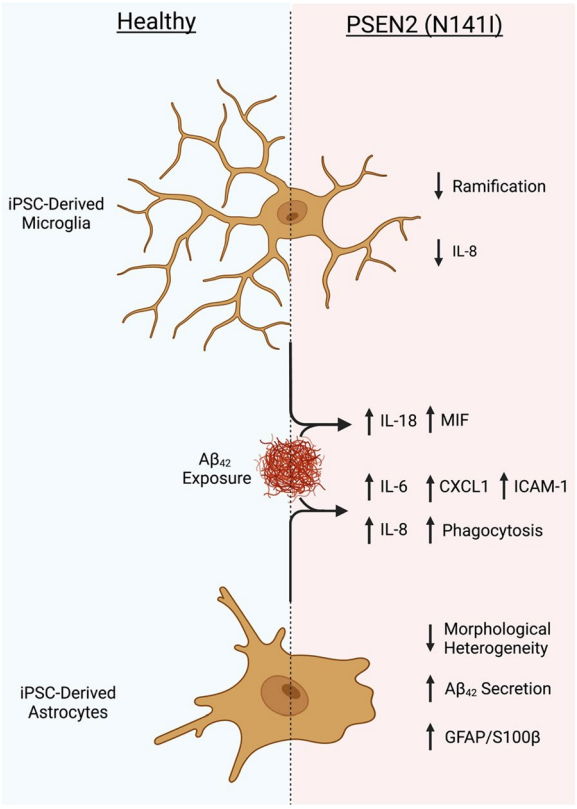

Fig. 11 Graphical representation and summary of morphological and immunological features of iPSC-derived microglia-like cells (top) and astrocytes (bottom) from healthy (left) and PSEN2 (N141I)-mutant fAD (right) origin. Created with Biorender.com

previously characterised method and producing cells positive for markers strongly consistent with microglial identity (IBA1 and TREM2) [46], we cannot conclusively infer bona fide microglial identity based solely on immunofluorescence staining as these proteins can be expressed on other myeloid cells such as monocytes and macrophages, hence our reference to these cells as microglia-like cells.

Changes in microglial and astrocyte morphology have been observed in the brain of AD patients and can reveal aspects about cellular phenotypes and reactivity states [47, 48]. Cell autonomous morphological changes in our AD-derived astrocytes mirror findings from iPSC-derived astrocytes from both sAD and fAD PSEN1-mutant origin, finding similar changes to astrocyte size, shape and morphological distribution [24]. Furthermore, triple transgenic and APP-mutant mouse models of AD also show reduction to astrocyte surface area, volume and process complexity, often before the onset of Aβ accumulation [49–51]. This suggests that the morphological changes associated with AD-derived astrocytes observed within the current study are not specific to the PSEN2 (N141I) mutation, but rather a common cell-autonomous dysfunction across multiple familial and sporadic origins which mirror those of reactive pro-inflammatory iPSC-derived astrocytes [52]. In addition to morphological changes, GFAP is widely used as a marker for aactivation [53] and is found to be upregulated in the brains of AD patients. Similarly, S100β expression is elevated in reactive astrocytes within the brains of AD patients and has been shown to have a direct relationship with reductions in stellate morphology [54–60]. Alongside the morphological characteristics, the increase in GFAP and S100β expression found within our AD-derived astrocytes suggests a basal skew towards a more reactive phenotype.

Similar to AD-derived astrocytes, iPSC-derived microglia-like cells from fAD patients showed a reduction in the number and complexity of processes extending from the glial cell body, however the length in which the processes are extending from the cell body seemed to be unchanged between disease groups. Various microglial morphologies have been defined using human post-mortem brain tissue, with each attributed to varying levels of reactivity [61]. It is suggested that under physiological conditions, microglia present with ramified, highly branched processes extending substantially from the cell body. In response to some damage signals, microglia transition into a morphology featuring less ramified, shorter and less complex processes [62], a characteristic observed in AD mouse models and in mice following ischaemic injury [63–65]. Similarly, PSEN2 (N141I) knock-in mice exhibited microglia with decreased ramification and number of dendritic branches, however no change in the branch length was observed [66, 67]. Despite PSEN2 (N141I)-mutant microglia presenting with some morphological characteristics consistent with microglial states common in neurodegenerative disease, namely reduced ramification, they do not entirely recapture the archetypal phenotype associated with these microglia and suggest a more subtle change in phenotype. However, whether these morphological features are replicated in PSEN2 (N141I)-mutant AD patients is unknown as no morphometric analysis has been conducted on human brain tissue.

A large body of evidence has implicated neuroinflammatory changes as a key neuropathological feature within AD progression, largely associated with changes in the states of astrocytes and microglia [13, 68, 69]. Unexpectedly, we found preliminary evidence that in iPSC-derived astrocytes the level of IL-6 secretion upon LPS stimulation was determined by APOE genotype and was independent of PSEN2 status. Within the CNS, APOE is a lipid transport protein acting as a ligand for low density lipoprotein receptor and primarily produced by astrocytes and is the highest genetic risk factor for sAD [1,

70]. In humans, APOE presents as three allelic variants (APOE ε2, APOE ε3 and APOE ε4) and compared to individuals with the APOE ε3/ε3 genotype, the APOE ε3/ε4 genotype confers around a threefold increase in risk of developing AD and is significantly overrepresented in individuals with sAD [71, 72]. A potential mechanism behind the disproportionate IL-6 response to LPS between APOE genotypes may lie within differences in the ability to bind to extracellular LPS. The single nucleotide polymorphism present within the APOE ε4 allele causes a reduction in the binding affinity of APOE to multiple extracellular proteins and LPS. As such, APOE ε3 binds to LPS with a higher affinity than the ε4 protein, reducing the ability of LPS to activate downstream pro-inflammatory cytokine production [73, 74]. This hypothesis suggests that the presence of the ε4 allele does not directly increase the pro-inflammatory activity of LPS, but rather is less effective than the ε3 allele at negatively regulating LPS-mediated neuroinflammation. Astrocytes isolated from APOE ε4 mice exhibited reduced astrogliosis and IL-6 production following LPS stimulation compared to astrocytes isolated from APOE ε3 mice [75, 76]. These findings are at odds with our data from iPSC-derived human astrocytes. This suggests that species differences may play a significant role in determining how the different isoforms of APOE mediate the response from astrocytes following neuroinflammatory stimulus.

We next examined the cytokine and chemokine profile of iPSC-derived astrocytes and microglia-like cells in response to exogenous $A\beta_{42}$, a more AD-relevant stimulus than LPS. We found that fAD-derived astrocytes exhibited an exaggerated release of IL-6 in response to $A\beta_{42}$, while variations in APOE genotypes had no significant effect. It is possible that any differences in the secretion of IL-6 between APOE genotypes within our cohort of iPSC-derived cells would be masked by the large effect observed with PSEN2 (N141I)-mutant lines. Future work utilising isogenic APOE lines will allow this to be investigated further.

Although IL-6 plays an important role in AD [77], the inflammatory profile of glial cells does not solely involve the level of IL-6 response, but rather the coordinated and unique secretion of multiple cytokines and chemokines. As such, the multi-cytokine array allowed us to analyse multiple cytokines simultaneously to gain a wider picture of the inflammatory profiles of AD-derived astrocytes and microglia-like cells. Both healthy and fAD-derived astrocytes basally secreted moderate levels of IL-8 while fAD-derived microglia-like cells exhibited a significant reduction in IL-8 secretion. Despite IL-8 being a pro-inflammatory cytokine [78], it also exhibits neurotrophic properties [79]. Hence, reductions in microglial IL-8 secretion could contribute to AD progression and neuronal damage through a reduction in neural reparative mechanisms. Upon exposure to $A\beta_{42}$, fAD-derived astrocytes exhibited significantly higher levels of ICAM-1, CXCL1, IL-6 and IL-8. In support of our findings, ICAM-1 is overexpressed by astrocytes in the brains of AD patients [80] and has been associated with Aβ pathology [81, 82]. Blood-brain barrier (BBB) dysfunctions have been identified as a key aspect of AD pathophysiology, to which astrocytes play an integral part [83]. Previous literature has shown extracellular ICAM-1 alters tight-junction integrity and integrin adhesiveness in vascular endothelial cells, resulting in increased BBB permeability [84–86]. A recent longitudinal study found elevated cerebrospinal fluid levels of ICAM-1, along with other cerebrovascular-associated proteins, in the preclinical, prodromal and dementia stages of AD [87]. Increased CXCL1 secretion was also found from Aβ-stimulated human astrocytes and was synaptotoxic in vitro [88]. In addition to the BBB, astrocytes form an integral part of cortical synapses and the overproduction of CXCL1 may underlie astrocyte-mediated synaptotoxicity. Taken together with previous literature, our results provide evidence that astrocytes may contribute to cerebrovascular and synaptic dysfunction at an early stage within AD progression through altered ICAM-1 and CXCL1 secretion in response to extracellular Aβ.

Similar to astrocytes, fAD-derived microglia-like cells showed an exaggerated increase of IL-8 from basal in response to $A\beta_{42}$. Significantly increased levels of the pro-inflammatory cytokines IL-18 and MIF upon $A\beta_{42}$ exposure were unique to fAD-derived microglia-like cells. Our results are consistent with previous data reporting increased IL-18 secretion from mouse microglia reacting to pro-inflammatory stimuli [89] and increased levels of IL-18 and MIF within the brains and cerebrospinal fluid of AD patients, respectively [90, 91]. In contrast to our findings, and these findings from human AD tissue, cultured microglia from PSEN2 (N141I) knock-in mice exhibited a different range of chemokine release in response to $A\beta_{42}$ not impacted in our PSEN2 (N141I)-derived microglia such as the significant upregulation of CCL2, CCL5 and CXCL1 [66]. Single-cell transcriptomic analysis highlight substantial species differences in microglial expression profiles and AD-associated genes such as PSEN [92, 93]. As such, species differences may underlie the disparities between findings and emphasises the need to study human glial cells in the context of AD.

In addition to contributing to increased $A\beta_{42}$ production, defective clearance of Aβ by glial cells is suggested

to play a role in the progression of AD pathophysiology [94] and is supported by previous work finding reduced uptake of $A\beta_{42}$ from PSEN1-mutant iPSC-derived astrocytes [27]. However, we found fAD-derived astrocytes to uptake significantly more $A\beta_{42}$ than healthy controls and suggest that phagocytic capacity may be impacted differentially by PSEN mutation status. Given the immunogenic properties of $A\beta_{42}$, the observed change in phagocytic profile in the current study is more reflective of stimulatory conditions. To better evaluate changes in the phagocytosis of iPSC-derived glia under basal/unstimulated conditions future work could involve the use of non-immunogenic substrates. The increased uptake of $A\beta_{42}$ in our fAD-derived astrocytes may be another exaggerated immune response upon exposure to $A\beta_{42}$, similar to our findings with $A\beta_{42}$-stimulated cytokine release. How the change in $A\beta_{42}$ uptake may contribute to AD progression is not clear. Perhaps the enhanced uptake of $A\beta_{42}$ may be initially neuroprotective, however as the disease progresses the cells become dystrophic and unable to perform continuous immune functions. In contrast to other studies modelling AD using TREM2 knock-out iPSC-derived microglia [45, 95, 96], our results suggest that fAD-derived microglia do not exhibit cell-autonomous deficits in Aβ uptake. Additionally, the results presented herein mirror the phagocytosis of Aβ reported in APP and PSEN1-mutant iPSC-derived microglia [25] and other factors such as neuron–microglia or astrocyte–microglia communication are likely to impact microglial phagocytosis and could change over the course of disease progression.

Taken together, a common feature between fAD-derived astrocytes and microglia-like cells was the exaggerated release of multiple pro-inflammatory cytokines in response to $A\beta_{42}$. Despite observing morphological characteristics in non-stimulated cells that were consistent with that of astrocytes and microglia responding to pro-inflammatory stimulus, AD-derived glial cells exhibited elevated levels of pro-inflammatory cytokines only in response to $A\beta_{42}$ and not basally. Our results suggests that unstimulated AD-derived astrocytes and microglia-like cells present with a primed phenotype, whereby the cells are predisposed to induce an exaggerated inflammatory response to a pathological stimulus.

Conclusion

In conclusion, we report the novel and successful differentiation of astrocytes and microglia-like cells from iPSCs harbouring an fAD-causative PSEN2 (N141I) mutation. These cells exhibit cell-autonomous morphological changes that are indicative of a basal skew towards a reactive phenotype and exaggerated pro-inflammatory cytokine/chemokine release upon immunological challenge. Additionally, AD-derived astrocytes showed elevated $A\beta_{42}$ uptake. The results presented here suggest that PSEN2 (N141I)-mutant glia present with a 'primed' phenotype whereby the exposure of $A\beta_{42}$ results in an exaggerated pro-inflammatory response. Whether the increased phagocytic capacity and elevated pro-inflammatory cytokine release from $A\beta_{42}$-stimulated astrocytes and microglia-like cells is detrimental to AD progression, or is initially neuroprotective but gains neurotoxic function as the disease progresses, is not known.

Abbreviations

AD	Alzheimer's disease
fAD	Familial Alzheimer's disease
sAD	Sporadic Alzheimer's disease
TREM2	Triggering receptor expressed on myeloid cells 2
APOE	Apolipoprotein
APP	Amyloid precursor protein
PSEN1	Presenilin 1
PSEN2	Presenilin 2
Aβ	Amyloid-beta
GFAP	Glial fibrillary acidic protein
iPSC	Induced pluripotent stem cell
TNF-α	Tumour necrosis factor-alpha
NPC	Neural progenitor cell
FGF2	Fibroblast growth factor 2
PBS	Phosphate buffer saline
NIM	Neural induction medium
DMEM	Dulbecco's Modified Eagle Medium
HPC	Hematopoietic progenitor cell
LPS	Lipopolysaccharide
CXCL1	Chemokine (C-X-C Motif) ligand 1
MIP	Macrophage inflammatory protein 1
MIF	Macrophage migration inhibitory factor
ICAM-1	Intracellular adhesion molecule 1
BBB	Blood brain barrier

Supplementary Information

The online version contains supplementary material available at https://doi.org/10.1186/s12974-023-02951-2.

Additional file 1: Supplementary Methods. **Table S1**. Primary antibodies used for immunofluorescence. **Table S2**. Secondary antibodies used for immunofluorescence. **Fig. S1.** Sanger sequencing chromatograms showing APOE genotyping of codon 112 (rs429358) and codon 158 (rs7412) for all iPSC lines. Yellow highlight indicates the position of the single nucleotide polymorphism. **Fig. S2.** Immunofluorescence images of iPSCs from three healthy control lines (Ctrl-06, Ctrl-71, Ctrl-88) and three familial AD lines harbouring a PSEN2 (N141I) mutation (fAD-08, fAD-948, fAD-950). The cells were stained for pluripotency markers Nanog (red), Oct 3 (green) and all nuclei were counterstained with DAPI (blue). Scale bars = 50 µm. **Fig. S3.** Immunofluorescence images of iPSC-derived NPCs from three healthy control lines (Ctrl-06, Ctrl-71, Ctrl-88) and three familial AD lines harbouring a PSEN2 (N141I) mutation (fAD-08, fAD-948, fAD-950). The cells were stained for **A** the neural progenitor markers Pax-6 (red) and Nestin (green), **B** a pluripotency marker Oct3 (green) and all nuclei were counterstained with DAPI (blue). Scale bars = 50 µm. **Fig. S4.** Immunofluorescence images of iPSC-derived astrocytes from three healthy control lines (Ctrl-06, Ctrl-71, Ctrl-88) and three familial AD lines harbouring a PSEN2 (N141I) mutation (fAD-08, fAD-948, fAD-950). The cells were stained for **A** astrocyte markers GFAP (red) and S100β (green), **B** the NPC marker nestin (green). All nuclei were counterstained with DAPI (blue). Scale bars = 50 µm. **Fig. S5.** Transcriptomic analysis of iPSC-derived cell types and primary human fetal astrocytes. **A** Principal component analysis and **B** cluster

analysis of iPSC-derived astrocytes (black) from healthy control lines (lines 06, 71 & 88) generated in our study and commercially-available primary astrocytes grown in our lab (green) combined with a datasets from Tcw et al (23), including primary astrocytes (purple), iPSC-derived NPCs (light blue), astrocytes (dark blue) and neurons (yellow). Contrast matrix of differential gene expression between cell types comparing datasets **C** our iPSC-derived astrocytes vs. Tcw et al's primary astrocyte and iPSC-derived neurons datasets, **D** Tcw et al's dataset alone, **E** our data alone. **Fig. S6** Immunofluorescence images of iPSC-derived microglia-like cells from three healthy control lines (Ctrl-06, Ctrl-71, Ctrl-88) and three familial AD lines harbouring a PSEN2 (N141I) mutation (fAD-08, fAD-948, fAD-950). Images show cells stained for **A** the microglial markers IBA1 (red), TREM2 (green), **B** CX3CR1 (red) and all nuclei were counterstained with DAPI (blue). Scale bars = 50 µm. **Fig. S7.** Multi-cytokine array of Alzheimer's or healthy iPSC-derived astrocytes **A** basally and **B** after 24 h exposure to 10 µM $A\beta_{42}$ and iPSC-derived microglia-like cells **C** basally and **D** after 24 h exposure to 10 µM $A\beta_{42}$. The figure displays the mean ± SD of three cell lines with the average of two experimental duplicates per line. Multiple unpaired, non-parametric Mann-Whitney t-tests adjusting for a 0.05 false discovery rate were used to test whether there were statistically significant differences between mean cytokine/chemokine release of AD-derived and healthy control astrocytes and microglia-like cells (*$p < 0.05$, **$p < 0.01$). Cytokines that yielded an average intensity value less than 10% of the maximum (represented by the dotted line) were considered background and not included in the statistical analysis. **Fig. S8.** Multi-cytokine array of APOE ε3/ε3 and APOE ε3/ε4 iPSC-derived astrocytes **A** basally and **B** after 24 h exposure to 10 µM $A\beta_{42}$ and iPSC-derived microglia-like cells **C** basally and **D** after 24 h exposure to 10 µM $A\beta_{42}$. The figure displays the mean ± SD of three cell lines with the average of two experimental duplicates per line. Multiple unpaired, non-parametric Mann–Whitney t-tests adjusting for a 0.05 false discovery rate were used to test whether there were statistically significant differences between mean cytokine/chemokine release of APOE ε3/ε3 and APOE ε3/ε4 astrocytes and microglia-like cells (*$p < 0.05$). Cytokines that yielded an average intensity value less than 10% of the maximum (represented by the dotted line) were considered background and not included in the statistical analysis. **Fig. S9.** Concentrations of **A** $A\beta_{42}$, **B** $A\beta_{40}$, **C** the ratio of $A\beta_{42:40}$ and **D** total Aβ protein quantified from iPSC-derived astrocyte supernatants 72 h after plating. Secreted Aβ concentrations were measured using a highly sensitive ELISA and normalised to total protein concentration determined by BCA. The figure displays the mean ± SD of three cell lines with $n \geq 2$ independent experiments per line. A post hoc unpaired *t*-test was used to test whether there were statistically significant differences between mean of APOE ε3/ε3 and APOE ε3/ε4 astrocytes.

Acknowledgements
The authors acknowledge the technical and scientific assistance of Sydney Microscopy & Microanalysis, the University of Sydney node of Microscopy Australia, as well as Sydney Analytical, a core research Facility at the University of Sydney, and the Sydney Informatics Hub. We also would like to acknowledge the NYSCF and Cedars-Sinai Medical Center's David and Janet Polak Foundation Stem Cell Core Laboratory providing the iPSC lines used within the study.

Author contributions
MAS contributed to the design of the work, acquisition of data, analysis of data, interpretation of data and drafted the manuscript. SDL, GGN and CM contributed to the acquisition of APOE genotyping data and revised the work. ADJM contributed to acquisition and analysis of the RNASeq data and drafted this portion of the manuscript. SRB and MS purified the amyloid and revised the work. AM contributed to acquisition and analysis of data. ELW conceived the work, contributed to the design of the work, contributed to the cell line acquisition and derivations, the interpretation of data and revised the work. MK contributed to the conception of the work and revised the work. All authors have read and approved the submitted version.

Funding
The authors' research is supported by a National Health and Medical Research Council of Australia (NHMRC) Program Grant (APP1132524). M.K is an NHMRC Principal Research Fellow (APP1154692).

Availability of data and materials
The datasets used during the current study are available from the corresponding authors on reasonable request.

Declarations

Ethics approval and consent to participate
Approval for the use of iPSCs was gained from the University of Sydney Institutional Biosafety Committee and Human Research Ethics Committee.

Consent for publication
Not applicable.

Competing interests
The authors declare that they have no competing interests.

Author details
[1]School of Medical Sciences, The Faculty of Medicine and Health, The University of Sydney, Camperdown, Australia. [2]School of Life and Environmental Sciences, Faculty of Science, The University of Sydney, Camperdown, Australia. [3]School of Chemistry, The Faculty of Science, The University of Sydney, Camperdown, Australia. [4]Central Clinical School, Faculty of Medicine and Health, The University of Sydney, Camperdown, Australia.

Received: 11 November 2022 Accepted: 7 November 2023
Published online: 04 January 2024

References

1. Bertram L, Tanzi RE. Genome-wide association studies in Alzheimer's disease. Hum Mol Genet. 2009;18(R2):R137–45.
2. D'Avanzo C, Aronson J, Kim YH, Choi SH, Tanzi RE, Kim DY. Alzheimer's in 3D culture: challenges and perspectives. BioEssays. 2015;37(10):1139–48.
3. De Jonghe C, Esselens C, Kumar-Singh S, Craessaerts K, Serneels S, Checler F, et al. Pathogenic APP mutations near the gamma-secretase cleavage site differentially affect Abeta secretion and APP C-terminal fragment stability. Hum Mol Genet. 2001;10(16):1665–71.
4. Selkoe DJ. Alzheimer's disease: genes, proteins, and therapy. Physiol Rev. 2001;81(2):741–66.
5. Jayadev S, Leverenz JB, Steinbart E, Stahl J, Klunk W, Yu CE, et al. Alzheimer's disease phenotypes and genotypes associated with mutations in presenilin 2. Brain. 2010;133(Pt 4):1143–54.
6. Ortiz-Virumbrales M, Moreno CL, Kruglikov I, Marazuela P, Sproul A, Jacob S, et al. CRISPR/Cas9-Correctable mutation-related molecular and physiological phenotypes in iPSC-derived Alzheimer's PSEN2 N141I neurons. Acta Neuropathol Commun. 2017;5(1):1–20.
7. Tanzi RE, Bertram L. Twenty years of the Alzheimer's disease amyloid hypothesis: a genetic perspective. Cell. 2005;120(4):545–55.
8. Lambert JC, Ibrahim-Verbaas CA, Harold D, Naj AC, Sims R, Bellenguez C, et al. Meta-analysis of 74,046 individuals identifies 11 new susceptibility loci for Alzheimer's disease. Nat Genet. 2013;45(12):1452–8.
9. Cagnin A, Brooks DJ, Kennedy AM, Gunn RN, Myers R, Turkheimer FE, et al. In-vivo measurement of activated microglia in dementia. Lancet. 2001;358(9280):461–7.
10. Hamelin L, Lagarde J, Dorothee G, Leroy C, Labit M, Comley RA, et al. Early and protective microglial activation in Alzheimer's disease: a prospective study using 18F-DPA-714 PET imaging. Brain. 2016;139(Pt 4):1252–64.
11. Funato H, Yoshimura M, Yamazaki T, Saido TC, Ito Y, Yokofujita J, et al. Astrocytes containing amyloid beta-protein (Abeta)-positive granules are associated with Abeta40-positive diffuse plaques in the aged human brain. Am J Pathol. 1998;152(4):983–92.
12. Kamphuis W, Middeldorp J, Kooijman L, Sluijs JA, Kooi EJ, Moeton M, et al. Glial fibrillary acidic protein isoform expression in plaque related astrogliosis in Alzheimer's disease. Neurobiol Aging. 2014;35(3):492–510.
13. Nagele RG, D'Andrea MR, Lee H, Venkataraman V, Wang HY. Astrocytes accumulate A beta 42 and give rise to astrocytic amyloid plaques in Alzheimer disease brains. Brain Res. 2003;971(2):197–209.

14. Senitz D, Reichenbach A, Smith TG Jr. Surface complexity of human neocortical astrocytic cells: changes with development, aging, and dementia. J Hirnforsch. 1995;36(4):531–7.
15. Dandrea MR, Reiser PA, Gumula NA, Hertzog BM, Andrade-Gordon P. Application of triple immunohistochemistry to characterize amyloid plaque-associated inflammation in brains with Alzheimer's disease. Biotech Histochem. 2001;76(2):97–106.
16. Ishizuka K, Kimura T, Igata-yi R, Katsuragi S, Takamatsu J, Miyakawa T. Identification of monocyte chemoattractant protein-1 in senile plaques and reactive microglia of Alzheimer's disease. Psychiatry Clin Neurosci. 1997;51(3):135–8.
17. Shao Y, Gearing M, Mirra SS. Astrocyte-apolipoprotein E associations in senile plaques in Alzheimer disease and vascular lesions: a regional immunohistochemical study. J Neuropathol Exp Neurol. 1997;56(4):376–81.
18. Drummond E, Wisniewski T. Alzheimer's disease: experimental models and reality. Acta Neuropathol. 2017;133(2):155–75.
19. Sloan SA, Darmanis S, Huber N, Khan TA, Birey F, Caneda C, et al. Human astrocyte maturation captured in 3D cerebral cortical spheroids derived from pluripotent stem cells. Neuron. 2017;95(4):779-90.e6.
20. Camp JG, Badsha F, Florio M, Kanton S, Gerber T, Wilsch-Brauninger M, et al. Human cerebral organoids recapitulate gene expression programs of fetal neocortex development. Proc Natl Acad Sci U S A. 2015;112(51):15672–7.
21. Abud EM, Ramirez RN, Martinez ES, Healy LM, Nguyen CHH, Newman SA, et al. iPSC-derived human microglia-like cells to study neurological diseases. Neuron. 2017;94(2):278-93.e9.
22. McQuade A, Coburn M, Tu CH, Hasselmann J, Davtyan H, Blurton-Jones M. Development and validation of a simplified method to generate human microglia from pluripotent stem cells. Mol Neurodegener. 2018;13(1):67.
23. Tcw J, Wang M, Pimenova AA, Bowles KR, Hartley BJ, Lacin E, et al. An efficient platform for astrocyte differentiation from human induced pluripotent stem cells. Stem Cell Reports. 2017;9(2):600–14.
24. Jones VC, Atkinson-Dell R, Verkhratsky A, Mohamet L. Aberrant iPSC-derived human astrocytes in Alzheimer's disease. Cell Death Dis. 2017;8(3): e2696.
25. Konttinen H, Cabral-da-Silva MEC, Ohtonen S, Wojciechowski S, Shakirzyanova A, Caligola S, et al. PSEN1DeltaE9, APPswe, and APOE4 confer disparate phenotypes in human iPSC-derived microglia. Stem Cell Rep. 2019;13(4):669–83.
26. Konttinen H, Gureviciene I, Oksanen M, Grubman A, Loppi S, Huuskonen MT, et al. PPARbeta/delta-agonist GW0742 ameliorates dysfunction in fatty acid oxidation in PSEN1DeltaE9 astrocytes. Glia. 2019;67(1):146–59.
27. Oksanen M, Petersen AJ, Naumenko N, Puttonen K, Lehtonen S, Gubert Olive M, et al. PSEN1 mutant iPSC-derived model reveals severe astrocyte pathology in Alzheimer's disease. Stem Cell Reports. 2017;9(6):1885–97.
28. Park J, Wetzel I, Marriott I, Dreau D, D'Avanzo C, Kim DY, et al. A 3D human triculture system modeling neurodegeneration and neuroinflammation in Alzheimer's disease. Nat Neurosci. 2018;21(7):941–51.
29. Guttikonda SR, Sikkema L, Tchieu J, Saurat N, Walsh RM, Harschnitz O, et al. Fully defined human pluripotent stem cell-derived microglia and tri-culture system model C3 production in Alzheimer's disease. Nat Neurosci. 2021;24(3):343–54.
30. Xu M, Zhang L, Liu G, Jiang N, Zhou W, Zhang Y. Pathological changes in Alzheimer's disease analyzed using induced pluripotent stem cell-derived human microglia-like cells. J Alzheimers Dis. 2019;67(1):357–68.
31. Lin YT, Seo J, Gao F, Feldman HM, Wen HL, Penney J, et al. APOE4 causes widespread molecular and cellular alterations associated with Alzheimer's disease phenotypes in human iPSC-derived brain cell types. Neuron. 2018;98(6):1141-54.e7.
32. Walsh DM, Thulin E, Minogue AM, Gustavsson N, Pang E, Teplow DB, et al. A facile method for expression and purification of the Alzheimer's disease-associated amyloid beta-peptide. FEBS J. 2009;276(5):1266–81.
33. Tian C, Liu Q, Ma K, Wang Y, Chen Q, Ambroz R, et al. Characterization of induced neural progenitors from skin fibroblasts by a novel combination of defined factors. Sci Rep. 2013;3:1345.
34. Liddelow SA, Barres BA. Reactive astrocytes: production, function, and therapeutic potential. Immunity. 2017;46(6):957–67.
35. Ao Z, Cai H, Wu Z, Song S, Karahan H, Kim B, et al. Tubular human brain organoids to model microglia-mediated neuroinflammation. Lab Chip. 2021;21(14):2751–62.
36. Liu W, Taso O, Wang R, Bayram S, Graham AC, Garcia-Reitboeck P, et al. Trem2 promotes anti-inflammatory responses in microglia and is suppressed under pro-inflammatory conditions. Hum Mol Genet. 2020;29(19):3224–48.
37. Ito D, Imai Y, Ohsawa K, Nakajima K, Fukuuchi Y, Kohsaka S. Microglia-specific localisation of a novel calcium binding protein, Iba1. Brain Res Mol Brain Res. 1998;57(1):1–9.
38. Franco-Bocanegra DK, Gourari Y, McAuley C, Chatelet DS, Johnston DA, Nicoll JAR, et al. Microglial morphology in Alzheimer's disease and after Abeta immunotherapy. Sci Rep. 2021;11(1):15955.
39. Davies DS, Ma J, Jegathees T, Goldsbury C. Microglia show altered morphology and reduced arborization in human brain during aging and Alzheimer's disease. Brain Pathol. 2017;27(6):795–808.
40. Young K, Morrison H. Quantifying microglia morphology from photomicrographs of immunohistochemistry prepared tissue using imageJ. J Vis Exp. 2018;136:e57648.
41. Brandenburg LO, Konrad M, Wruck CJ, Koch T, Lucius R, Pufe T. Functional and physical interactions between formyl-peptide-receptors and scavenger receptor MARCO and their involvement in amyloid beta 1–42-induced signal transduction in glial cells. J Neurochem. 2010;113(3):749–60.
42. Xu X, Lei Y, Luo J, Wang J, Zhang S, Yang XJ, et al. Prevention of beta-amyloid induced toxicity in human iPS cell-derived neurons by inhibition of Cyclin-dependent kinases and associated cell cycle events. Stem Cell Res. 2013;10(2):213–27.
43. Ferreira A, Sinjoanu RC, Nicholson A, Kleinschmidt S. Abeta toxicity in primary cultured neurons. Methods Mol Biol. 2011;670:141–53.
44. Veeraraghavalu K, Zhang C, Zhang X, Tanzi RE, Sisodia SS. Age-dependent, non-cell-autonomous deposition of amyloid from synthesis of beta-amyloid by cells other than excitatory neurons. J Neurosci. 2014;34(10):3668–73.
45. McQuade A, Kang YJ, Hasselmann J, Jairaman A, Sotelo A, Coburn M, et al. Gene expression and functional deficits underlie TREM2-knockout microglia responses in human models of Alzheimer's disease. Nat Commun. 2020;11(1):5370.
46. Bottcher C, Schlickeiser S, Sneeboer MAM, Kunkel D, Knop A, Paza E, et al. Human microglia regional heterogeneity and phenotypes determined by multiplexed single-cell mass cytometry. Nat Neurosci. 2019;22(1):78–90.
47. Carpenter AF, Carpenter PW, Markesbery WR. Morphometric analysis of microglia in Alzheimer's disease. J Neuropathol Exp Neurol. 1993;52(6):601–8.
48. Vehmas AK, Kawas CH, Stewart WF, Troncoso JC. Immune reactive cells in senile plaques and cognitive decline in Alzheimer's disease. Neurobiol Aging. 2003;24(2):321–31.
49. Beauquis J, Pavia P, Pomilio C, Vinuesa A, Podlutskaya N, Galvan V, et al. Environmental enrichment prevents astroglial pathological changes in the hippocampus of APP transgenic mice, model of Alzheimer's disease. Exp Neurol. 2013;239:28–37.
50. Kulijewicz-Nawrot M, Verkhratsky A, Chvatal A, Sykova E, Rodriguez JJ. Astrocytic cytoskeletal atrophy in the medial prefrontal cortex of a triple transgenic mouse model of Alzheimer's disease. J Anat. 2012;221(3):252–62.
51. Olabarria M, Noristani HN, Verkhratsky A, Rodriguez JJ. Concomitant astroglial atrophy and astrogliosis in a triple transgenic animal model of Alzheimer's disease. Glia. 2010;58(7):831–8.
52. Hyvarinen T, Hagman S, Ristola M, Sukki L, Veijula K, Kreutzer J, et al. Co-stimulation with IL-1beta and TNF-alpha induces an inflammatory reactive astrocyte phenotype with neurosupportive characteristics in a human pluripotent stem cell model system. Sci Rep. 2019;9(1):16944.
53. Escartin C, Guillemaud O, Carrillo-de Sauvage MA. Questions and (some) answers on reactive astrocytes. Glia. 2019;67(12):2221–47.
54. Simpson JE, Ince PG, Lace G, Forster G, Shaw PJ, Matthews F, et al. Astrocyte phenotype in relation to Alzheimer-type pathology in the ageing brain. Neurobiol Aging. 2010;31(4):578–90.
55. Kashon ML, Ross GW, O'Callaghan JP, Miller DB, Petrovitch H, Burchfiel CM, et al. Associations of cortical astrogliosis with cognitive performance and dementia status. J Alzheimers Dis. 2004;6(6):595–604; discussion 73–81.

56. Griffin WS, Stanley LC, Ling C, White L, MacLeod V, Perrot LJ, et al. Brain interleukin 1 and S-100 immunoreactivity are elevated in Down syndrome and Alzheimer disease. Proc Natl Acad Sci U S A. 1989;86(19):7611–5.
57. Mrak RE, Sheng JG, Griffin WS. Correlation of astrocytic S100 beta expression with dystrophic neurites in amyloid plaques of Alzheimer's disease. J Neuropathol Exp Neurol. 1996;55(3):273–9.
58. Sheng JG, Mrak RE, Griffin WS. S100 beta protein expression in Alzheimer disease: potential role in the pathogenesis of neuritic plaques. J Neurosci Res. 1994;39(4):398–404.
59. Marshak DR, Pesce SA, Stanley LC, Griffin WS. Increased S100 beta neurotrophic activity in Alzheimer's disease temporal lobe. Neurobiol Aging. 1992;13(1):1–7.
60. Brozzi F, Arcuri C, Giambanco I, Donato R. S100B protein regulates astrocyte shape and migration via interaction with Src kinase: implications for astrocyte development, activation and tumor growth. J Biol Chem. 2009;284(13):8797–811.
61. Torres-Platas SG, Comeau S, Rachalski A, Bo GD, Cruceanu C, Turecki G, et al. Morphometric characterization of microglial phenotypes in human cerebral cortex. J Neuroinflammation. 2014;11:12.
62. Colonna M, Butovsky O. Microglia function in the central nervous system during health and neurodegeneration. Annu Rev Immunol. 2017;35:441–68.
63. Salobrar-Garcia E, Rodrigues-Neves AC, Ramirez AI, de Hoz R, Fernandez-Albarral JA, Lopez-Cuenca I, et al. Microglial activation in the retina of a triple-transgenic Alzheimer's disease mouse model (3xTg-AD). Int J Mol Sci. 2020;21(3):816.
64. Baron R, Babcock AA, Nemirovsky A, Finsen B, Monsonego A. Accelerated microglial pathology is associated with Abeta plaques in mouse models of Alzheimer's disease. Aging Cell. 2014;13(4):584–95.
65. Leyh J, Paeschke S, Mages B, Michalski D, Nowicki M, Bechmann I, et al. Classification of Microglial Morphological Phenotypes Using Machine Learning. Front Cell Neurosci. 2021;15: 701673.
66. Nam H, Lee Y, Kim B, Lee JW, Hwang S, An HK, et al. Presenilin 2 N141I mutation induces hyperactive immune response through the epigenetic repression of REV-ERBalpha. Nat Commun. 2022;13(1):1972.
67. Fung S, Smith CL, Prater KE, Case A, Green K, Osnis L, et al. Early-onset familial Alzheimer disease variant PSEN2 N141I heterozygosity is associated with altered microglia phenotype. J Alzheimers Dis. 2020;77(2):675–88.
68. Kinney JW, Bemiller SM, Murtishaw AS, Leisgang AM, Salazar AM, Lamb BT. Inflammation as a central mechanism in Alzheimer's disease. Alzheimers Dement (N Y). 2018;4:575–90.
69. Heppner FL, Ransohoff RM, Becher B. Immune attack: the role of inflammation in Alzheimer disease. Nat Rev Neurosci. 2015;16(6):358–72.
70. Grehan S, Tse E, Taylor JM. Two distal downstream enhancers direct expression of the human apolipoprotein E gene to astrocytes in the brain. J Neurosci. 2001;21(3):812–22.
71. Liu CC, Liu CC, Kanekiyo T, Xu H, Bu G. Apolipoprotein E and Alzheimer disease: risk, mechanisms and therapy. Nat Rev Neurol. 2013;9(2):106–18.
72. Corder EH, Saunders AM, Strittmatter WJ, Schmechel DE, Gaskell PC, Small GW, et al. Gene dose of apolipoprotein E type 4 allele and the risk of Alzheimer's disease in late onset families. Science. 1993;261(5123):921–3.
73. den Hartigh LJ, Altman R, Hutchinson R, Petrlova J, Budamagunta MS, Tetali SD, et al. Postprandial apoE isoform and conformational changes associated with VLDL lipolysis products modulate monocyte inflammation. PLoS ONE. 2012;7(11): e50513.
74. Hatters DM, Budamagunta MS, Voss JC, Weisgraber KH. Modulation of apolipoprotein E structure by domain interaction: differences in lipid-bound and lipid-free forms. J Biol Chem. 2005;280(40):34288–95.
75. Maezawa I, Maeda N, Montine TJ, Montine KS. Apolipoprotein E-specific innate immune response in astrocytes from targeted replacement mice. J Neuroinflammation. 2006;3:10.
76. Ophir G, Meilin S, Efrati M, Chapman J, Karussis D, Roses A, et al. Human apoE3 but not apoE4 rescues impaired astrocyte activation in apoE null mice. Neurobiol Dis. 2003;12(1):56–64.
77. Fraga VG, Magalhaes CA, Loures CMG, de Souza LC, Guimaraes HC, Zauli DAG, et al. Inflammatory and pro-resolving mediators in frontotemporal dementia and Alzheimer's disease. Neuroscience. 2019;421:123–35.
78. Ehrlich LC, Hu S, Sheng WS, Sutton RL, Rockswold GL, Peterson PK, et al. Cytokine regulation of human microglial cell IL-8 production. J Immunol. 1998;160(4):1944–8.
79. Araujo DM, Cotman CW. Trophic effects of interleukin-4, -7 and -8 on hippocampal neuronal cultures: potential involvement of glial-derived factors. Brain Res. 1993;600(1):49–55.
80. Akiyama H, Kawamata T, Yamada T, Tooyama I, Ishii T, McGeer PL. Expression of intercellular adhesion molecule (ICAM)-1 by a subset of astrocytes in Alzheimer disease and some other degenerative neurological disorders. Acta Neuropathol. 1993;85(6):628–34.
81. Verbeek MM, Otte-Holler I, Westphal JR, Wesseling P, Ruiter DJ, de Waal RM. Accumulation of intercellular adhesion molecule-1 in senile plaques in brain tissue of patients with Alzheimer's disease. Am J Pathol. 1994;144(1):104–16.
82. Rozemuller JM, Eikelenboom P, Pals ST, Stam FC. Microglial cells around amyloid plaques in Alzheimer's disease express leucocyte adhesion molecules of the LFA-1 family. Neurosci Lett. 1989;101(3):288–92.
83. Noe CR, Noe-Letschnig M, Handschuh P, Noe CA, Lanzenberger R. Dysfunction of the Blood-Brain Barrier-A Key Step in Neurodegeneration and Dementia. Front Aging Neurosci. 2020;12:185.
84. Nielsen HM, Londos E, Minthon L, Janciauskiene SM. Soluble adhesion molecules and angiotensin-converting enzyme in dementia. Neurobiol Dis. 2007;26(1):27–35.
85. Clark PR, Manes TD, Pober JS, Kluger MS. Increased ICAM-1 expression causes endothelial cell leakiness, cytoskeletal reorganization and junctional alterations. J Invest Dermatol. 2007;127(4):762–74.
86. Rentzos M, Michalopoulou M, Nikolaou C, Cambouri C, Rombos A, Dimitrakopoulos A, et al. The role of soluble intercellular adhesion molecules in neurodegenerative disorders. J Neurol Sci. 2005;228(2):129–35.
87. Janelidze S, Mattsson N, Stomrud E, Lindberg O, Palmqvist S, Zetterberg H, et al. CSF biomarkers of neuroinflammation and cerebrovascular dysfunction in early Alzheimer disease. Neurology. 2018;91(9):e867–77.
88. Perez-Nievas BG, Johnson L, Beltran-Lobo P, Hughes MM, Gammallieri L, Tarsitano F, et al. Astrocytic C-X-C motif chemokine ligand-1 mediates beta-amyloid-induced synaptotoxicity. J Neuroinflammation. 2021;18(1):306.
89. Prinz M, Hanisch UK. Murine microglial cells produce and respond to interleukin-18. J Neurochem. 1999;72(5):2215–8.
90. Nasiri E, Sankowski R, Dietrich H, Oikonomidi A, Huerta PT, Popp J, et al. Key role of MIF-related neuroinflammation in neurodegeneration and cognitive impairment in Alzheimer's disease. Mol Med. 2020;26(1):34.
91. Ojala J, Alafuzoff I, Herukka SK, van Groen T, Tanila H, Pirttila T. Expression of interleukin-18 is increased in the brains of Alzheimer's disease patients. Neurobiol Aging. 2009;30(2):198–209.
92. Srinivasan K, Friedman BA, Etxeberria A, Huntley MA, van der Brug MP, Foreman O, et al. Alzheimer's patient microglia exhibit enhanced aging and unique transcriptional activation. Cell Rep. 2020;31(13): 107843.
93. Monaco G, van Dam S, Casal Novo Ribeiro JL, Larbi A, de Magalhaes JP. A comparison of human and mouse gene co-expression networks reveals conservation and divergence at the tissue, pathway and disease levels. BMC Evol Biol. 2015;15:259.
94. Mawuenyega KG, Sigurdson W, Ovod V, Munsell L, Kasten T, Morris JC, et al. Decreased clearance of CNS beta-amyloid in Alzheimer's disease. Science. 2010;330(6012):1774.
95. Reich M, Paris I, Ebeling M, Dahm N, Schweitzer C, Reinhardt D, et al. Alzheimer's risk gene TREM2 determines functional properties of new type of human iPSC-derived microglia. Front Immunol. 2020;11: 617860.
96. Hall-Roberts H, Agarwal D, Obst J, Smith TB, Monzon-Sandoval J, Di Daniel E, et al. TREM2 Alzheimer's variant R47H causes similar transcriptional dysregulation to knockout, yet only subtle functional phenotypes in human iPSC-derived macrophages. Alzheimers Res Ther. 2020;12(1):151.

Publisher's Note